NORTHWESTERN
UNIVERSITY

Electrical Engineering and Computer Science Department

Technical Report
NWU-EECS-11-04
May 1, 2011
Multi-Pole Field Persistent Routing with Bounded Delay in Wireless Sensor Networks

Oliviu C. Ghica[1] Goce Trajcevski[1] Marco Zuniga[2]
Rene Schubotz[2] Peter Scheuermann[1] Manfred Hauswirth[2]

(1) Department of Electrical Engineering and Computer Science
Northwestern University
Evanston, IL, USA
(2) Digital Enterprise Research Institute
National University of Ireland
Galway, Ireland

Abstract

This work addresses the problem of balancing the spatial distribution of the routing-load among the nodes in a given sensor network and the tradeoff that can be achieved for providing certain level of quality of service (QoS) guarantees. For high-density networks, several studies have proposed field-based routing paradigms to uniformly distribute the traffic load throughout the network. However, as network density decreases, we observe major shortcomings of the current state-of-the-art: (i) path-merging leads to a reduction of path diversity, and (ii) the paths directed towards the border of the network merge into a single path along the border. These path merging effects decrease significantly the energy balance, and as consequence, the lifetime of the network. In this article, we propose a novel mechanism to enable better load balancing for single-source and multiple-source scenarios, while minimizing the cost of the tradeoff for bounding the end-to-end packet delivery latencies. Our evaluations demonstrate that by using the proposed methodology, the network lifetime can be significantly prolonged, when long-term point-to-point queries are considered.

Keywords: Wireless Sensor Networks, Multipath Routing, Lifetime, QoS.

Multi-Pole Field Persistent Routing with Bounded Delay in Wireless Sensor Networks

Oliviu C. Ghica, Goce Trajcevski,* Peter Scheuermann†
Department of EECS
Northwestern University
Evanston, Il 60208
{ocg474,goce,peters}@eecs.northwestern.edu

Marco Zuniga, Rene Schubotz, Manfred Hauswirth
Digital Enterprise Research Institute
National University of Ireland
Galway, IRL
{rene.schubotz, marco.zuniga, manfred.hauswirth}@deri.org

Abstract

This work addresses the problem of balancing the spatial distribution of the routing-load among the nodes in a given sensor network and the tradeoff that can be achieved for providing certain level of quality of service (QoS) guarantees. For high-density networks, several studies have proposed field-based routing paradigms to uniformly distribute the traffic load throughout the network. However, as network density decreases, we observe major shortcomings of the current state-of-the-art: (i) path-merging leads to a reduction of path diversity, and (ii) the paths directed towards the border of the network merge into a single path along the border. These path merging effects decrease significantly the energy balance, and as consequence, the lifetime of the network. In this article, we propose a novel mechanism to enable better load balancing for single-source and multiple-source scenarios, while minimizing the cost of the tradeoff for bounding the end-to-end packet delivery latencies. Our evaluations demonstrate that by using the proposed methodology, the network lifetime can be significantly prolonged, when long-term point-to-point queries are considered.

1 Introduction

The problem of routing in wireless sensor networks (WSN) has received a considerable attention [4] and, in particular, the problem of multipath routing has been of interest for two complementary goals: (1) increasing the reliability of the delivery and aggregates computation [37]; and (2) balancing the load among the nodes [20, 36, 43, 57]. When it comes to load-balancing, which is the focus of this work, the multipath paradigm alleviates the problem inherent to single-path routing – uneven utilization of the energy reserves which, as an important consequence, affects the lifetime of WSNs [14].

For a given sink, the two basic kinds of multipath routing scenarios are: (1) single-source; and (2) multiple-sources [44, 39, 41, 6, 53, 31, 29], In addition to the energy consumptions due to packets forwarding, in multiple-sources settings, an important energy consumption factor is due to MAC collisions at the spatio-temporal intersection of paths from different sources. In this context, the field-based routing [41, 31] has been identified as an efficient energy balancing mechanism for both single and multiple source scenarios. The essence of field-based routing is that the sink is assigned a negative charge, while the sources are assigned positive charges, and multiple routes are based on individual gradients of the field, providing a wider range for paths, which thereby reducing utilization hot-spots. With all the importance and potential benefits of the field-based routing paradigm, we observe two important drawbacks:

*Research supported by the NSF-CNS 0910952
†Research partially supported by the NSF-IIS-0325144

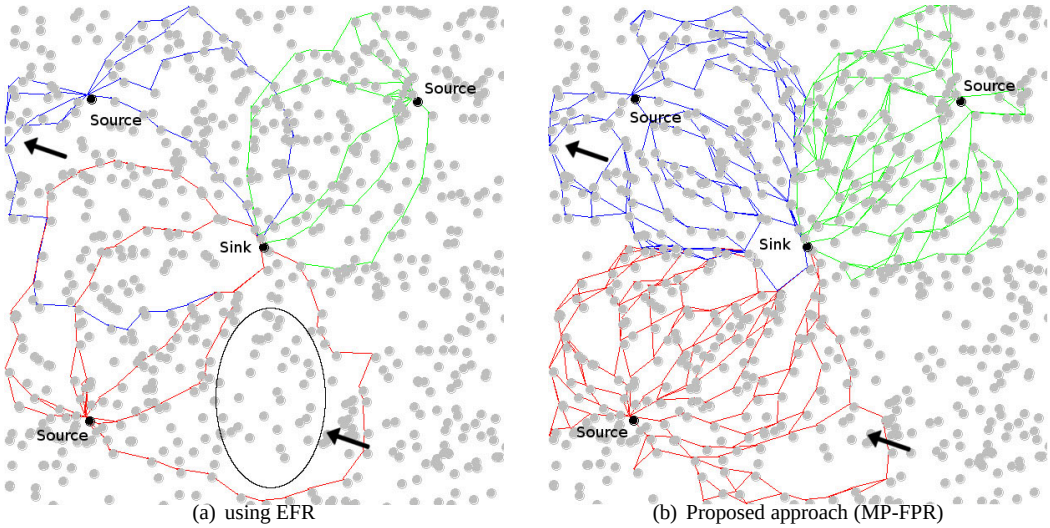

(a) using EFR (b) Proposed approach (MP-FPR)

Figure 1: Paths merging in multipath routing

(1) the paths around the boundary of the network tend to merge, significantly reducing the extent of load-balancing at the edges of the network; (2) while there is a potentially infinite number of gradient-based routes, the number actually available paths is limited by the sparsity of the neighboring nodes. As an illustration, Figure 1(a) shows how the EFR-based routing completely fails to utilize portions of the network (e.g., the ellipse-bound area), and causes paths-merging (e.g., the boundary) – both of which are reduced in the settings in Figure 1(b).

Analogies to various branches of Physics are often encountered in designing and analyzing communication networks. The field of wireless sensor networks is particularly supportive of such analogies when it comes to efficient routing design, since both physical phenomena and sensor nodes poses strong spatial correlations. An comprehensive survey of recent solutions that are based on analogies to physics can be found in [51]. For example, application of fluid dynamic modelling has been employed for solving network flow problems [3], or the basics of electrostatic theory has been often invoked as the key for optimal distribution of traffic [52, 31]. Other areas of Physics include diffusion theory, for efficient routing [27, 26], percolation theory, for capacity and connectivity assessment in sensor networks [16, 19], and particle flux theory for traffic load evaluations [44]. When it comes to the problem of lifetime extension in wireless sensor networks, efficient distribution of traffic is paramount, therefore, solutions that are based on principles of electrostatic theory can be pursued.

There are two orthogonal approaches to routing via analogy to electrostatic theory in the research community. One analogy relies on Thomson's theorem, which focuses on the analogies to the distribution of electric charges on physical conductors at an equilibrium configuration; the goal is to devise an optimal placement for a set of electrostatic point-charges, and by analogy, an optimal placement of multiple corresponding sources and sinks in the physical field, along with the optimal distribution of the traffic between them such that the length of the point-to-point routes are minimized, considering limited degree of freedom for both source and sinks. An instance of this analogy is presented in [52]. The second type of approach focuses on the properties of the electrostatic field created between multiple fixed point-charges for the purpose of relaying point-to-point data in an multipath-approach, such as in EFR (Electrostatic Field Routing) [41]. The work comprised in this article aligns with the latter approach, where certain electrostatic field properties are being exploited for providing route isolation among multiple families of point-to-point routes, as well as even distribution of routes in the network for improved load-balancing.

1.1 The Shortcomings of EFR

Many of the results that are related to the optimal arrangement of the network traffic in sensor networks via analogies to Physics are described from a macroscopic perspective, i.e. rely on the assumption of massively large, dense and boundless networks. This is because such results are better formalized through macroscopic quantities such as node density and volume of traffic at each point in space, rather than via node-level references. Consequently, under

macroscopic modelling approaches, there always exists a practical difficulty of mapping individual sensor nodes to real phenomenon, which is seldom ignored. Electrostatic field approaches are also analyzed predominantly from a macroscopic perspective.

Approaches such as EFR do attempt to bridge the gap between macroscopic and microscopic modelling by providing a novel forwarding scheme to realize the mapping between discrete sensor nodes to a discrete subset of electrostatic field lines. In EFR, the goal is to achieve a multipath routing scheme that is both distributed and stateless for the purpose of improving scalability, robustness and higher delivery ratio as compared to other comparable approaches: LAR, DREAM, GPSR and AOMDV.

We observe that EFR promotes path redundancy, but not *path diversity* – a quantitative metric describing the ”richness” of path-families in terms of distinct point-to-point routes – consequently, EFR’s path diversity is relatively poor in all but highly dense and uniformly distributed networks, as observed experimentally during our evaluations. This aspect critically distinguishes EFR from the approach proposed in this article, which considers path diversity and distribution of paths around the source and sink nodes to be paramount for the effectiveness of load balancing and consequent lifetime gains.

EFR framework is also oblivious to the existence of network boundaries, which is an important element from a load-balancing standpoint. Specifically, electrostatic field routing is particularly susceptible to boundary nodes being overloaded. This is because the electrostatic field is theoretically infinite, therefore the load associated with a subset of the field lines that span outside of network boundaries will be carried over by the boundary relay nodes. The network boundary problem has been previously recognized in the research community. For example, Kalantari *et al.* [31] proposes a centralized solution for the boundary problem, that requires a-priori information about traffic demands and node positions. In a similar line of work, Toumpis and Tassiulas [52] show that an optimal placement of nodes between a set of sources and sinks can be used to solve boundary problems. Our work, however, distinguishes from these approaches in the sense that boundary problems are addressed in an innovative way, within the same framework of electrostatic field theory and with minimal overhead in terms of packet size increase and computational effort [52].

1.2 Outline of Contributions

The main contributions of the work comprised in this article consist of an improved mechanism that enable rich path-diversity characteristics in arbitrarily dense network settings, considering realistic finite physical coverage with well defined network bounds. Additionally, an route-control framework is introduced to enable satisfiability of certain quality of service (QoS) requirements. Specifically, four novel mechanisms are being introduced:

- Field Persistent Forwarding for path-diversity improvement under a multitude of conditions, including lower density and non-uniform distributions,
- Method of Images for boundary effects resolution,
- Multi-Pole Routing Protocol for charge information management, and
- Virtual charges-based framework for QoS control.

The subsequent Sections are organized as follows. Section 2.1 provides the necessary background information on Electrostatic Theory. Section 2.2 presents the network model this work builds upon. The specifics of the EFR protocol are presented in Section 2.3, and, by comparison, the novel field persistency and accurate field line forwarding mechanism are introduced in Section 3.1. The Method of Images is presented in Section 3.2, and the multi-pole routing protocol for charge allocation and management is analyzed in Section 3.3. The QoS-control framework based on virtual charges is presented in Section 3.4. The experimental evaluation is presented in Section 3.5, followed by related work in Section 4 and concluding remarks in Section 5.

2 Preliminaries

Before presenting the main contributions of this work, it is necessary to introduce the background on electrostatic theory. In addition, we outline the network model along with the underlying assumptions that are being made, and

overview lower level information regarding the EFR approach, in order to comparatively illustrate the benefits and various design choices that form the basis of the newly proposed Field Persistent Routing. Additionally, the *discrepancy* of a point-set – a measure of the node's distributions – needs to be formally defined as it represents an important practical dimension for algorithmic performance evaluation.

2.1 Overview of Electrostatic Theory

Electrostatics is the branch of science that deals with the phenomena arising from stationary electric charges. More specifically, electrostatic phenomena arise from the forces that electric charges exert on each other. Such forces exercised between two *point-charges* are described by Coulomb's law, which states that the magnitude of the electrostatic force between two point electric charges Q_1 and Q_2 is directly proportional to the product of the magnitudes of each charge and inversely proportional to the square of the Euclidean distance between their locations:

$$F = \frac{Q_1 Q_2}{4\pi r^2 \varepsilon_0} \tag{1}$$

where ε_0 is a constant called the *permittivity of vacuum*.

The *electric field* (in units of volt per meter) at any given point is defined as the force (in Newtons) per unit charge q (in Coulombs) at that point:

$$\vec{E} = \frac{\vec{F}}{q} \tag{2}$$

From this definition and Coulomb's law, it follows that the magnitude of the electric field E created by a single point charge Q at distance r from its location is:

$$E(r) = \frac{Q}{4\pi r^2 \varepsilon_0} \tag{3}$$

A discrete distribution of N static particle charges Q_i with respective positions $\mathbf{r}_i \in \mathbb{R}^2$ produces an electrostatic field $\overrightarrow{\mathbf{E}}$, typically visualized as a set of *field lines*. Essentially, each field line corresponds to a trajectory that a unit charge Q_u would follow in a given field, depending on the initial location and direction-vector that Q_u has with respect to the other charges in that field. The electrostatic potential ϕ_E at point $\mathbf{r} \in \mathbb{R}^2$ is given by:

$$\phi_E(\mathbf{r}) = \frac{1}{4\pi\varepsilon_0} \sum_{i=1}^{N} sgn(Q_i) \frac{Q_i}{|\mathbf{r}_i - \mathbf{r}|} \tag{4}$$

where $\mathbf{r}_i$ $(1 \leq i \leq N)$ are the locations of the charges in the field. Electric field lines originate at positive charges and converge towards negative charges. For any particular charge Q_i, the function $sgn(Q_i)$ returns the polarity of charge Q_i.

In our settings, each of the charges will correspond to one of the multiple end-points of point-to-point routes in the sensor network. By convention, routes carry the information flow originating at the source nodes towards the sink, correspondingly, we adopt the convention that Q_{snk} charges associated to sink nodes are negatively charged, i.e. $sgn(Q_{snk}) = -1$, whereas the charges associated with each source node are positive, i.e. $sgn(Q_{src}) = 1$. This equation allows one to evaluate the magnitude E of a point charge in the electric field of N distinct charges $Q_i, i = 1 \ldots N$ via superposition. Specifically, the curve along which a given node sn_k, located at $r = L_k$, with a radius-vector to the location of the source L_{src} and sink L_{snk} denoted as $\mathbf{r}_i \in \mathbb{R}^2$, is determined based on the electric field at $\mathbf{r}_i$. Using Equation 4, this is given by:

$$\mathbf{E}(\mathbf{r}) = \frac{1}{4\pi\varepsilon_0} \sum_{i=1}^{N} sgn(i) \frac{Q_i}{|\mathbf{r}_i - \mathbf{r}|^3} (\mathbf{r}_i - \mathbf{r}) \tag{5}$$

In electrostatics, the electric field $\mathbf{E}$ can be visualized discretely as a set of *curves* which indicate the direction of the field vector at any given point. Figure 2 gives a visual interpretation of a sample electrostatic field with two point-charges of opposite polarity. We reiterate that, assuming the end-points of a point-to-point communication in

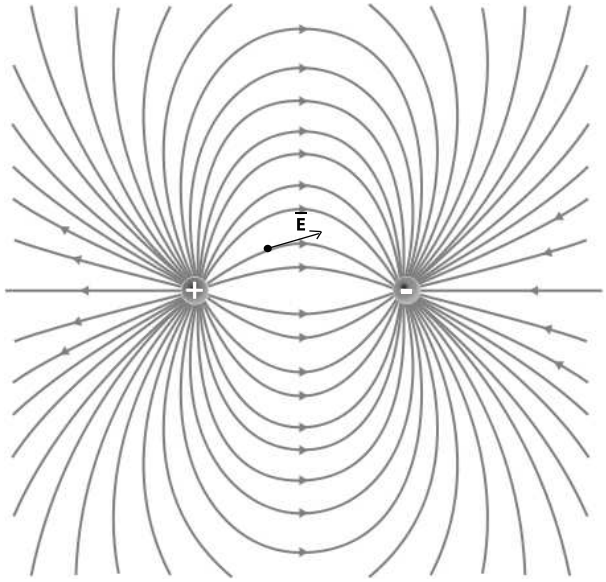

Figure 2: Sample electrostatic field determined by two point charges of opposite polarity

wireless sensor network coincide with the physical location of the point-charges, the electrostatic field lines can be readily used as alternative guiding "trajectories" for multiple path routing.

An additional advantage that electric field lines provide over the existing geometric trajectories approaches can be outlined in multiple sink-source settings. For example, Figure 3 shows the electrostatic field generated by multiple point-charges that are present in the same field. This is but an illustration of the following two important properties:

- Self-Adjustment Property. Field lines are uniquely determined by the existing set of charges in the field, hence their distribution in the physical field naturally changes as new charges are added, without any explicit trajectory parametrization; for example, the central set of field lines in Figure 3 is visibly more constrained within a tighter physical area when compared to the case depicted in Figure 2, due to the effects of the two additional pairs of charges;

- Disjointness Property. Field lines connecting different end-points are naturally disjoint; as it can be observed in Figure 3, none of the field lines intersect, rather, marginal field lines are deflected around other central field lines.

The consequence of the self-adjustment property is that one can easily control the spread of the field lines by means of strategically placing additional charges in the physical field – a property that forms the basis of two of the main contributions of this work: (1) the *method of images* and (2) enabling QoS control. The disjointness property enables efficient generation of distinct and non braiding families of alternative routes pertaining to multiple source-sink scenarios. Namely, it is sufficient to properly assign point-charges correspondent to the specific source and sink sensor nodes, and the set of resulting fields lines are already updated in the new distribution and can be readily used for routing purposes, based on localized application of the electric field equation 5.

2.2 Network Model

A wireless sensor network consists of a homogeneous set $SN = \{sn_1, sn_2, \ldots, sn_N\}$ of N sensor nodes that are deployed over a given area of interest. The nodes have the capabilities of self-organizing, in a cooperative manner[48][1], and form a connected network. Each node $sn_i \in SN$ occupies a unique, static physical location in the 2D cartesian space, represented as a pair $< x_i, y_i >$ of coordinates along along the X and Y axis. We assume that the location of a

[1]The non-cooperative (selfish) behavior of sensor nodes it is beyond the scope of this article.

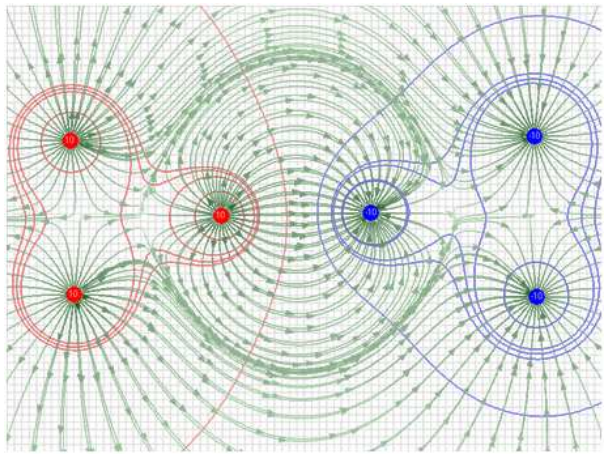

Figure 3: Sample electrostatic field with multiple point charges

sensor node is provided by an on-board GPS device[2], or by implementing a lightweight localization service [23, 9] or discovery algorithm [40, 17, 46, 8].

Each node is equipped with a small omnidirectional radio device that can be used to establish communication links with other nodes. We assume a unit-disk communication model, where R_c represents the communication range of a given sensor node. In practice, the effective communication range R_c^* may be lower, i.e. $R_c^* < R_c$, due to environmental obstructions or other non-deterministic spatial conditions .Due to the limited spatial coverage of the radio antenna, each node $sn_i \in SN$ can communicate directly with only a subset of nodes from the network, i.e. the *neighbors* of node sn_i. We denote the set of *neighbors* of a node $sn_i \in SN$ as $NB_i = \{sn_j \in SN | \, \|sn_i, sn_j\| \leq R_c\}$, where $\|sn_i, sn_j\|$ is the Euclidian distance between nodes sn_i and sn_j. Each node can determine the position of its 1-hop neighbors through a periodic location information exchange mechanism.

Energy-wise, each sensor node is powered by a finite energy resource, such as a battery, and has the capability of powering off the radio equipment to save energy during inactive periods. The wake-up coordination does not make the subject of the work comprised in this article, however wake-up coordination solutions, either software-based [28], or hardware-based (Remotely Activated Switch [12]), [5], are readily available.

Sensor nodes can act both as a *relay* and a *source* of sensed data. Users formulate queries specifying properties of the data stream that is to be collected from a particular geographic location, and submit them via *sink* nodes, which act gateways between the user and the sensor network. Queries are relayed to specific nodes in charge of their processing, i.e. the source nodes, and the resulting, possibly long-term, data stream is collected and relayed back to the sink. To promote workload balancing, multiple paths are established between the source and sink end-points, and the transmission of individual packets alternates among the different paths.

From a deployment area perspective, it is additionally being assumed that the network's boundaries are known or can be determined via an appropriate protocol, e.g. [13]. Without loss of generality, the parametric shape of the network is assumed to be rectangular.

2.3 Overview of Electrostatic-Field Based Routing (EFR)

The electrostatic field-based routing is a form of trajectory-based routing, where trajectories are represented as electric field lines. The field lines originate at source nodes and lead towards designated sink nodes. In order for a sensor node to know how to route a packet all it needs to know is the location and corresponding electrostatic charges information corresponding to the source and sink nodes, as well as its own location relative to them.

In principle, EFR selects a discrete subset of field lines (out of the infinite number of them) that can be established between a given *(source, sink)* pair, and constructs routes along them. We refer to this set S_f as a family of paths. Figure 4(a) illustrates a family of field lines established between a source and a sink node. Each field line in S_f is

[2]The MTS420CA Mica Mote board from Crossbow Technology Inc is an example of a GPS equipped sensor node

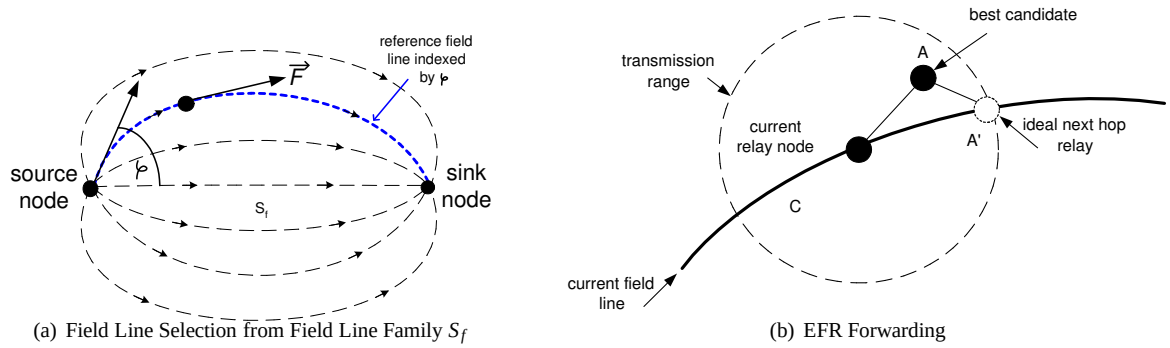

(a) Field Line Selection from Field Line Family S_f (b) EFR Forwarding

Figure 4: (a) Initially the source selects an angle φ to route the packet. This angle determines the *path* to be followed. (b) The current relay node C uses its residency field line and maximum transmission range to determine the optimum position of an ideal relay node A', and picks a real neighboring relay node A close to A';

uniquely identified by the value of the angle φ_j, determined by the *tangent* to a given/chosen field line at the source, and the line segment between the source and the sink[3] . For example, assuming a uniform selection of the tangential-angle from the interval $[0, \pi]$, a particular field line φ_j can be chosen from a field line set $S_f = \{k\frac{2\pi}{N_r} \mid k = \overline{1, N_r}\}$, where N_r represents the desired cardinality of the family of routes S_f. For each data-packet, the source node arbitrarily selects one of the outbound field lines to forward the packet along. Each such field line is identified by the tangential angle φ to the field line at the source node, as illustrated in Figure 4(a) [4]. Along the route, the forwarding decision takes in the consideration: (1) the relative proximity of the available relay nodes to the a particular field line of interest, and (2) the communication range margins in order to minimize hop count along a field line. Figure 4(b) illustrates the route selection and forwarding process in EFR.

During forwarding, each relay node takes in consideration its physical location and the electrostatic field line it physically resides onto (the *residency* field line) as a reference for the forwarding decision. The important observation is that, due to finite nodes' densities, the residency field line may not necessarily coincide with the original field line φ picked by the source node, or any of the field lines the up-stream nodes used for forwarding.

EFR relies on a simple, angle-based heuristic, to select the next relay node. Specifically, each current relay node calculates the tangent to the residency field line θ_C evaluated at the location of the node, and selects the farthest neighboring node that exhibits a bounded deviation $\theta_\varepsilon = 15^\circ$ from the tangent, i.e. physically located within the resulting sector area, as illustrated in Figure 5. It is important to observe, however, that node D in Figure 5, although closest to field line, it is not selected by EFR. From an end-to-end routing perspective, EFR's heuristic leads to path deviations from the original field line. Under highly dense networks, however, such deviations are limited and paths are maintained in some vicinity of the original field line. The path deviation effect is exemplified in Figure 6, which depicts the actual mapping of relay nodes and the resulting path in more practical settings with lower density of nodes. Following Section details the critical limitations of the EFR protocol under practical settings.

2.4 Limitations of EFR

From a lifetime perspective, a major drawback of the EFR forwarding heuristic is its predisposition to *path merging* effects – the primary source for energy consumption hot-spots via relay nodes sharing and overload. There are three main causes for path merging effects:

- Path Deviation
- Field Line Drifting
- Network Boundaries Effects

[3]Note that the cardinality of the S_f, as well as the criteria for selecting a particular φ_j can be user-specified.

[4]The tangent to a point in the field is actually evaluated on an infinitely small disk, in 2D, or sphere, in 3D cases, centered at that particular point

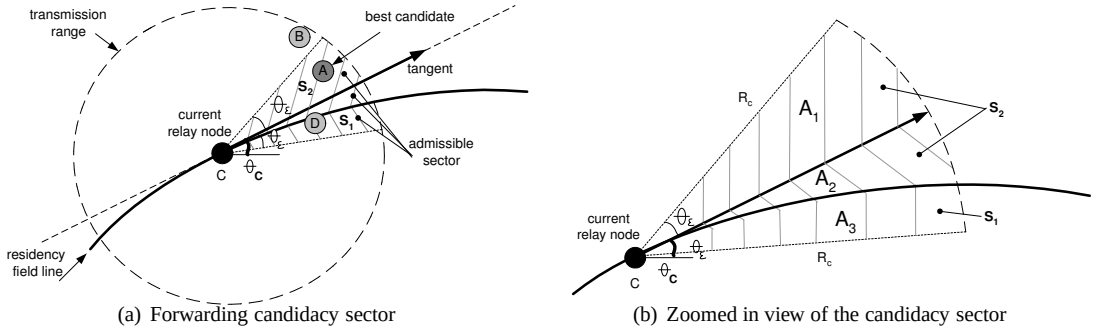

(a) Forwarding candidacy sector

(b) Zoomed in view of the candidacy sector

Figure 5: EFR's angular forwarding criteria. (a) EFR selects node A as the next relay node, because it is farther away from the current relay C than D is. Although it is the farthest relay node from C, node B does not meet the angular criteria to become a feasible candidate node. (b) In this scenario, if ∂S_1 represents the area of S_1 region, then $\partial S_1 = \partial A_3$, $\partial S_2 = \partial A_1 + \partial A_2$

Path Deviation. As briefly outlined in Section 2.3, path deviation is the result of finite nodes densities, as candidate relay nodes are unlikely to be found exactly along a certain field line. EFR's angular forwarding criteria greatly aids constraining path deviation, however, as the density of field lines actively used for routing increases, or the density of neighboring sensor candidates decreases, such path deviations can become severe and, in practical settings, lead to conditions in which relay nodes carry traffic associated with multiple adjacent field lines. Figure 7 exemplifies the path deviation and path merging problems.

Field Line Drifting. Field line drifting represents a permanent path deviation, where the residency field line continuously changes as a direct consequence of path deviations. Field line drifting is more apparent as the length of the routes increases. Recalling the forwarding criteria outlined in Figure 5, the angular candidacy sector is virtually divided by the curved field line in two disjoint regions, namely S_1 and S_2. Following the notations in Figure 5(b), if ∂A_1 represents the area of region A_1, then $\partial A_1 = \partial A_2 + \partial A_3$. Consequently, $\partial S_1 = \partial A_1 + \partial A_2$ and $\partial S_2 = \partial A_3 = \partial S_1 - \partial A_2$, hence $\partial S_2 - \partial S_1 = \partial A_3 > 0$. The essential conclusion is that these two sectors have uneven areas, and for this particular setting, $\partial S_2 > \partial S_1$. Assuming a uniform distribution of nodes and that the probability of finding candidate relay nodes within each sector S_1 and S_2 is proportional with the area of each sector, i.e. $P_{S_2} = \kappa \cdot \partial S_2$ and $P_{S_1} = \kappa \cdot \partial S_1$, for some constant κ, then $P_{S_2} > P_{S_1}$. This implies a general trend of outward drift toward a longer adjacent field line.

Boundary Effects. Path deviation and ultimately field line drifting can also be caused by the network boundaries, as the load associated with different field lines that cross the boundaries of the network is commonly carried by the boundary nodes. This is an inward type of field line drift. Figure 9(a) illustrates a scenario with three field lines, two of which are crossing out boundaries. As it can be observed, the three different paths corresponding to the field lines merge at the boundary of the network and persist as a merged path until downstream towards the sink node, regardless whether original field lines return within the coverage area. This overloads not only boundary nodes, but also inside nodes in the proximity of the sink node. In comparison, Figure 9(b) illustrates the performance of the proposed alternative to EFR in comparable conditions. As it can be observed, it is possible to obtain no field line drifting effects and any temporarily merged routes due to physical limitations can and should be re-mapped to the original field lines whenever possible. This desideratum is achieved by the proposed *field persistency mechanism*, which will be discussed next.

Multiple concurrent field line drifts can lead to permanent path merging effects, as illustrated in Figure 7. As it can be observed, paths remained merged downstream of the merging point since they become commonly defined by the residency field line of their common relay. Consequently, field line drifting effectively reduces path diversity, and ultimately the energy consumption distribution.

Figure 8 illustrates actual path assignments, in a simulated environment, comparatively among the current state of the art routing, namely EFR, and MP-FPR – the novel mechanisms presented in this article. It is important to observe both in-network behavior in terms of field line drifting and path-merging, as well as the boundary effects. As a specific example, EFR attains a much poorer path diversity around source and (sink) nodes, for the following reason: in EFR, the paths selected by a source node are dictated by the residency field lines of its 1-hop neighbors, which is an

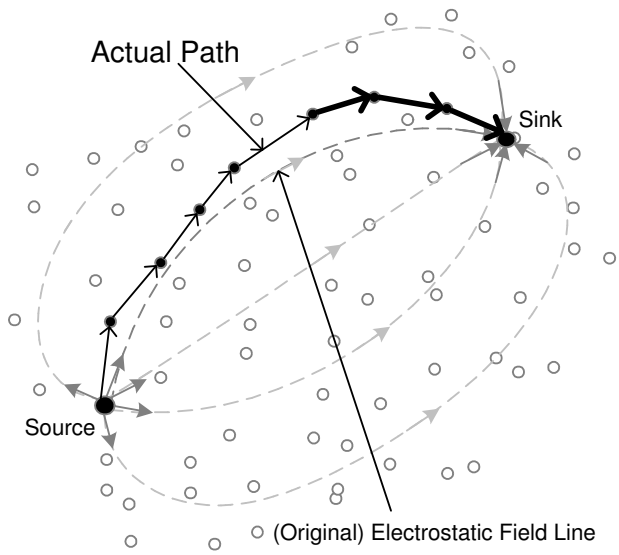

Figure 6: Mapping of routes to electrostatic field lines with EFR routing. Due to finite distributions, the actual route cannot be precisely mapped to a field line and, in reality, it deviates

example of field-line drifting at the source. Hence, the number of outgoing paths is effectively limited to the number of neighbor nodes. In Figure 9(b) it can be observed that 4 different paths that are directed towards the edge merge into a single path along the edge.

3 Efficient Load Balancing via Field Persistency

We now proceed with explaining in greater detail the forwarding algorithm that is used by the nodes as a heuristic to guide the selection of the next relay nodes from among a set of available neighbors. As previously mentioned, the aim is to ”force” the routing nodes to spread (in a spatial sense) the number of possible routes, thereby adapting the shape of the multiple routes to the changes in the spatial distribution. Subsequently, the approach that improves the existing solutions for balancing the energy-consumption when routing near the boundary of the network (cf. [41, 31]) is presented. Lastly, a protocol that addresses charge allocation and management, route construction and QoS correlation is presented.

3.1 Field Persistent Routing

Field persistent routing is enabled by two complementary mechanisms:

- Reference field line retention
- Accurate field-line forwarding (minimal field-line deviation forwarding)

which are detailed in sequel.

3.1.1 Reference Field Line Retention

For a given route, we denote as the ”reference” field line the electric field line chosen initially by the source node to be used for establishing a route towards the sink. This distinguishes from ”residency” field line, as the later represents any arbitrary field line that physically intersects a specific sensor node (the resident). Ideally, the reference and residency

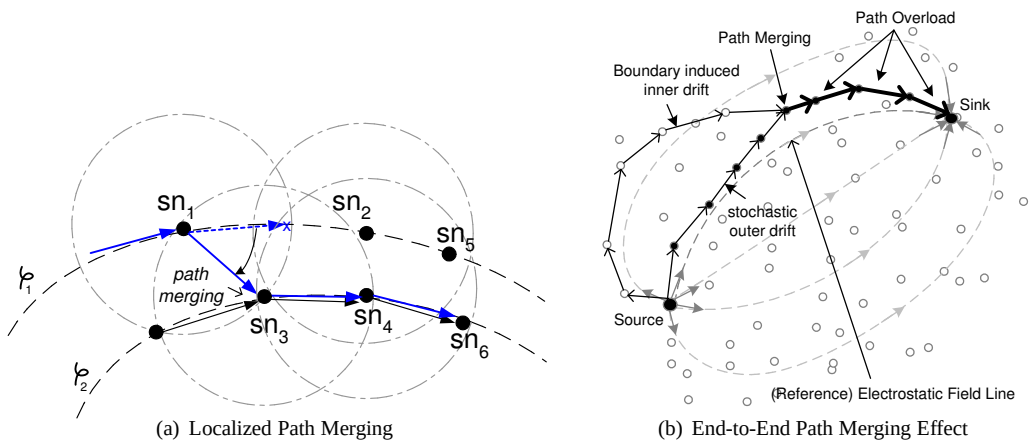

(a) Localized Path Merging (b) End-to-End Path Merging Effect

Figure 7: Illustration of path deviation and path merging with EFR's forwarding model. (a) Low-level view of the path-merging effect. According to the gradient at node sn_1 along a field line φ_1, the next-hop is supposed to be node sn_2. However, since node sn_2 is out of range of sn_1, node sn_3 is selected instead. Subsequently, node sn_4 is selected as next-hop of sn_3 and so on. Assuming that nodes sn_3 and sn_4 are already servicing another electrostatic field line φ_2, this phenomena has a detrimental consequence on load balancing: while node sn_3 and its successors are overloaded, node sn_2 and its successors remain unutilized. (b) Corresponding high-level view of the path-merging effect

field lines along an entire route should coincide, however, in reality, this need not be the case due to finite nodes densities.

Reference field line retention is a mechanism by which a forwarding node "remembers" the reference field line and continuously attempts to redirect the route along it, if that path has been deviated. Figure 10(a), which represents a zoomed-in portion of the Figure 10(b), illustrates the process, which distinguishes our MP-FPR methodology from the original EFR (cf. Figure 7(a) and 7(b) respectively). Depending on networks conditions, paths merging cannot always be avoided, however, we aim at ensuring a remediation whenever the network conditions allow it. Specifically, consider node sn_1 in Figure 10(a) as the current relay node. The ideal next-hop node that it would select (illustrated with location sn_x), would be the one located at the intersection of the circle bounding sn_1's communication range, and the gradient curve φ_1 to which sn_1 belongs. According to EFR provisions, since there exists no real physical node at that exact location, a nearby node sn_2 is selected instead because: (1) it is furthest away towards the sink; and (2) it is closest to the original route[5] of the field-line determined by φ_1 at sn_1, as opposed to, e.g., sn_2. When node sn_5 becomes a current relay, under a reference field line retention policy, it will use the known reference field line information (either φ_1 of φ_2), rather than the residency field line, to forward along the iso-contour of φ_1 or φ_2, i.e. to nodes sn_6 or sn_7 respectively. Effectively, in MP-FPR, a path splitting decision takes place at node sn_5, relieving portion of the load on the downstream nodes from sn_5 – which is the critical difference from EFR.

To accomplish this, clearly, some extra information needs to be "embedded" in the transmitted packets. That information is actually the "identity" of the reference curve as determined by the source, which is being retained by the forwarding nodes. In reality, a source node has only a finite number of 1-hop neighbors that can be used for generating multiple paths. Hence, the field-line of each neighbor is used as an index for the family of routes that can be generated from that particular source. To enumerate the field-lines, we use the value of the tangent angle φ (cf. Figure 4(a)) to the respective curves (i.e., the direction of the gradient to the equi-potential curves) at the source.

With respect to Figure 10(a), the immediate benefits of the MP-FPR mechanisms can be intuitively explained as: (1) EFR would have "forgotten" that node sn_5 is the closest node to the original field-line; (2) EFR would have double-loaded nodes like sn_3, sn_4 and sn_5 – because both routes would follow the same actual path. The overhead associated with retention of the reference field line is insignificant, at least comparing with the load-balancing benefits it attains as the experiments will demonstrate, since one extra byte per packet is sufficient to encode 256 different reference

[5]We note that in the original work [41], a bound is placed on the angle that the next-hop can have with respect to the tangent (i.e., the direction of $\overline{F}_1$) at sn_1.

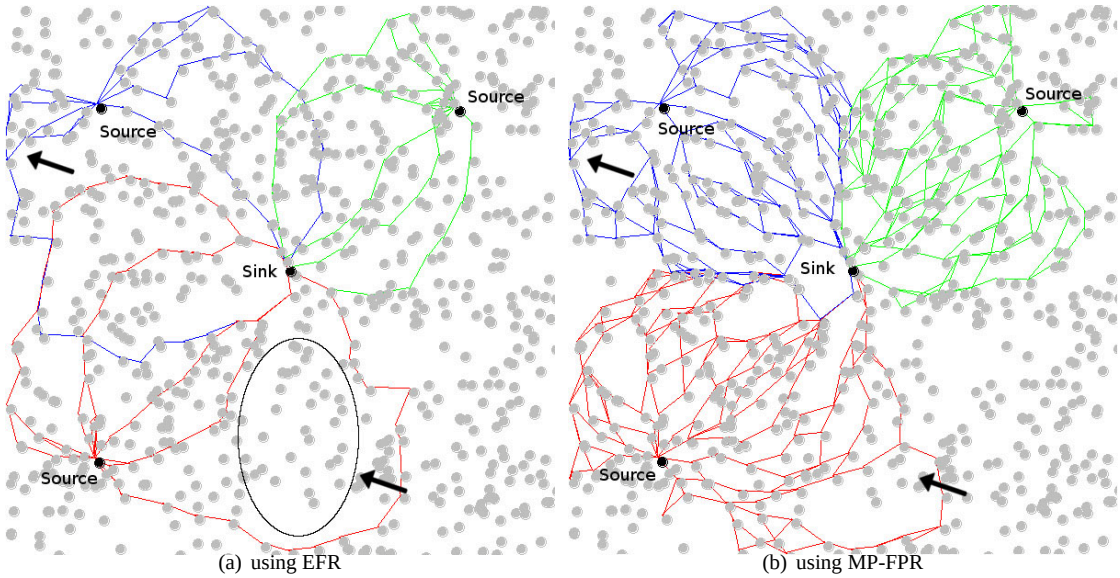

(a) using EFR (b) using MP-FPR

Figure 8: Comparison of the state-of-the-art EFR and the novel alternative, MP-FPR. (a) EFR (i) fails to utilize a significant fraction of the network's resources (bottom ellipse) and (ii) has undesirable path merging effects at the boundaries of the network (upper-left arrow). (b) MP-FPR corrects these 2 shortcomings.

lines, a sufficient number for many practical purposes.

3.1.2 Accurate Field Line Forwarding

Let $\Phi(p_A) = \varphi_A$ be a function that returns the index φ_A of the residency field line of an arbitrary point p_A in the 2D cartesian system. Specifically, given a point p_A, the $\Phi(p_A)$ returns the angle of the electric field vector evaluated on the same field line at the origin of the field, as illustrated in Figure 4(a).

Field persistent forwarding mechanism aims to minimize the deviation from a given reference field line φ. This mechanism prevents path merging and ensures re-splitting of any merged path whenever feasible. Accordingly, minimal deviation can be achieved if the downstream relay nodes are chosen in a manner that minimizes the field index difference between the *resident* and the *reference* field lines. Specifically, assume that NB_c denotes the set of 1-hop neighbors of a relay node sn_c that prepares to forward a data packet. The electrostatic field line index $\Phi(L_{sn_i})$ evaluated at the location L_{sn_i} of each of the candidate nodes $sn_i \in NB_c$, based on successive applications of relationship 5, and the residency field line index φ of the reference field line, can be used to identify the best candidate node sn_k via the following expression:

$$sn_k = \Gamma(sn_i, sn_c, \varphi) \triangleq Argmin_{sn_i \in NB_c} \{|\Phi(L_{sn_i}) - \varphi|\} \tag{6}$$

where the resident field line of a given node sn_k can be determined based on the: (1) location and charge of the source(s); (2) location and charge of the sink; and (3) its own location.

Equation 6 captures the essence of FPR operations, enabling accurate assessment of any field line deviation. This equation, however, is not sufficient, as it does not comprise traffic flow information, i.e. direction, which is needed for ensuring continuous forwarding progress towards the sink. Namely, a decision taken solely on Equation 6 is susceptible to local minima effects and can lead to routing loops. For example, assume two sequential relay nodes $sn_i \in NB_j$ and $sn_j \in NB_i$, such that $\{sn_i, sn_j\} \in NB_j \bigcap NB_i$. Let $\Delta_f(sn_k, \varphi)$ represent a measure of the deviation of node sn_k from the reference field line φ, defined as:

$$\Delta_f(sn_k, \varphi) = \left|\Phi(L_{sn_k}) - \varphi\right| \tag{7}$$

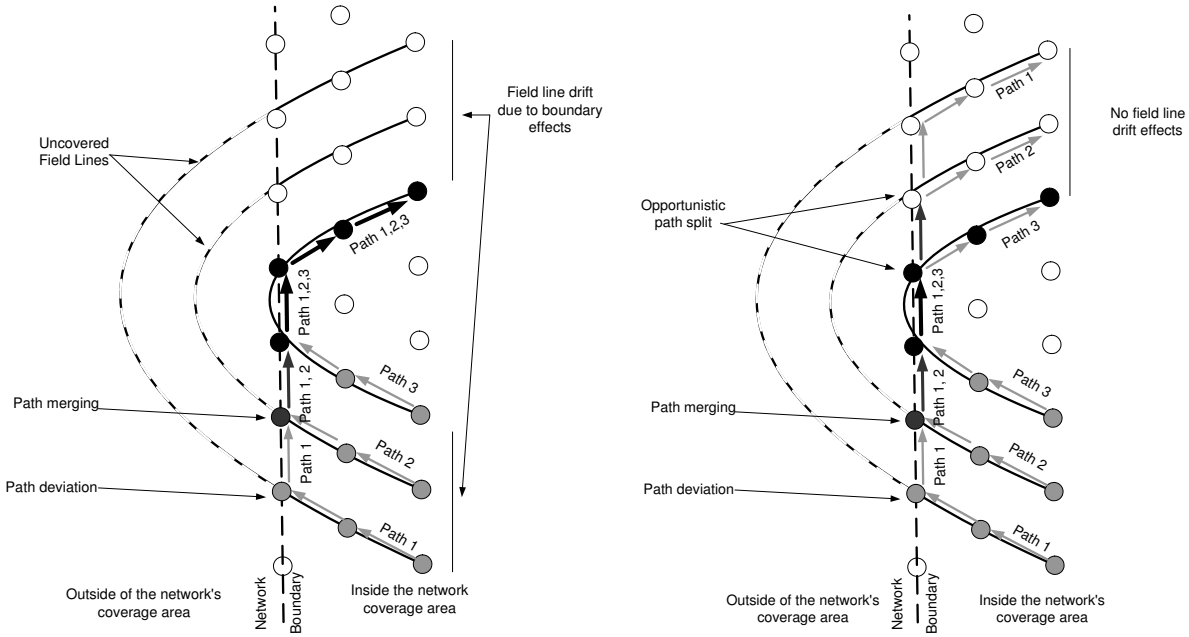

(a) using EFR (b) using MP-FPR

Figure 9: Impact of boundary effects over the path diversity of the network

where $\Phi(L_{sn_k})$ represents the index of the residency field line of sensor node sn_k. If $\Delta_f(sn_i,\varphi) < \Delta_f(sn_k,\varphi), \forall sn_k \in NB_i \cup NB_j \setminus \{sn_j\}$ and $\Delta_f(sn_j,\varphi) < \Delta_f(sn_k,\varphi), \forall sn_k \in NB_i \cup NB_j \setminus \{sn_i\}$, then nodes sn_i and sn_j will form a routing cycle, since according to Equation 6, $\Gamma(sn_i,\varphi) = sn_j$, and $\Gamma(sn_j,\varphi) = sn_i$.

To enable forwarding progress evaluation, a progress metric needs to be defined. Assuming that sn_c is the current relay node, let $L_{mpp}(\varphi)$ denote the *ideal* cartesian coordinate where a sensor node should be located for optimal forwarding decision, i.e. providing no field line deviation and maximum progress/advancement with respect to the direction of packet flow along field line φ. We refer to $L_{mpp}(\varphi)$ as the *maximal progress point*. Accordingly, the deviation from the maximal progress point can be defined as follows:

$$\Delta_p(sn_i, sn_c, \varphi) = \|sn_i, L_{mpp}(sn_c, \varphi)\| \tag{8}$$

where $\|sn_i, L_{mpp}(\varphi)\|$ represents Euclidean distance.

Equations 7 and 8 define the two deviation metrics that form the foundation of FPR's accurate forwarding mechanism. To formalize the forwarding decision, a cost function can be defined based on normalized variants of the two deviation metrics. Specifically, Δ_f can be expressed relative to the minimum and maximum resident field line index difference of all the field lines that intersect the communication range R_c of a current sensor node sn_c, as illustrated in Figure 11(a), or deviation from the maximum progress point, as illustrated in Figure 11(b). Following the notations from Figure 11(a), i.e. P_{out} and P_{inn} represent the two orthogonal extremities of the communication range relative to the direction of the resident field vector of a current relay node sn_c, $\Phi(P_{out}) = \varphi_{out}$ and $\Phi(P_{inn}) = \varphi_{inn}$ the corresponding field line indexes at the extremities of the communication range, then the normalized field line deviation function can be defined as:

$$\overline{\Delta}_f(sn_i, sn_c, \varphi) = \begin{cases} \left|1 - \frac{\varphi_{out} - \Phi(sn_i)}{\varphi_{out} - \varphi}\right|, \text{if} \Phi(sn_i) > \varphi \\ \left|1 - \frac{\Phi(sn_i) - \varphi_{inn}}{\varphi - \varphi_{inn}}\right|, \text{if} \Phi(sn_i) \leq \varphi \end{cases} \tag{9}$$

and the maximum progression deviation as:

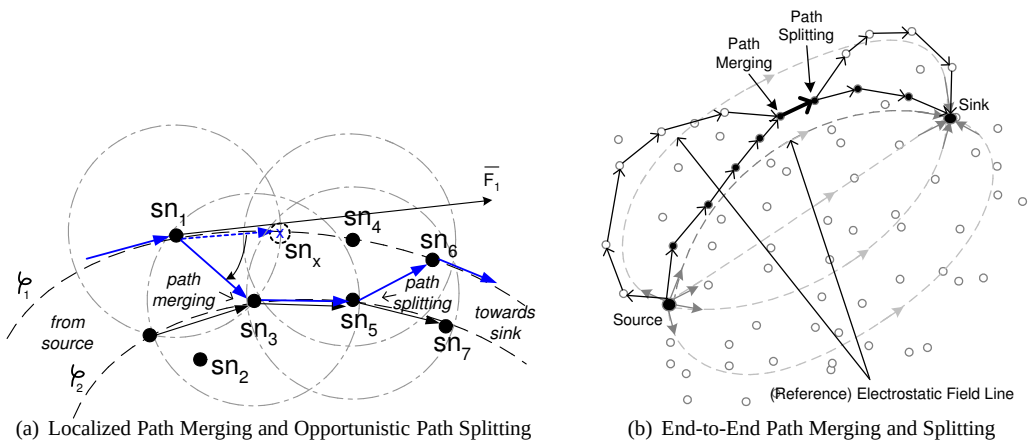

(a) Localized Path Merging and Opportunistic Path Splitting (b) End-to-End Path Merging and Splitting

Figure 10: Illustration of path merging and opportunistic path splitting with MP-FPR forwarding model. (a) Low-level view of the path-merging and splitting. Due to low density of nodes, node sn_1 diverts traffic associated to the reference field line φ_1 through sn_2 and path merging occurs, since sn_2 already serves another field lines φ_2; it is only at node sn_4 where there exists an opportunity of splitting the paths back by alternatively forwarding to sn_5 and sn_6 the associated flows (b) Corresponding high-level view of the path-merging and path splitting

$$\overline{\Delta}_p(sn_i, sn_c, \varphi) = \frac{\|sn_i, L_{mpp}(sn_c, \varphi))\|}{2R_c} \tag{10}$$

where R_c represents the communication range.

Consider sn_c a current sensor node that executes the forwarding decision, and NB_c the candidate list of 1-hop neighbor nodes. Based on $\overline{\Delta}_f$ and $\overline{\Delta}_p$, a cost function can be defined and associated with each candidate node $sn_i \in NB_c$ to penalize both deviations from the progress along a field line, as well as deviations from the reference field line itself, given by the geographical location of sn_i, as follows:

$$\eta(sn_i, sn_c, \varphi) = \beta_f \overline{\Delta}_f(sn_i, sn_c, \varphi) + \beta_p \overline{\Delta}_p(sn_i, sn_c, \varphi) \tag{11}$$

This cost function effectively establishes a tradeoff between the two deviations when no candidate node is located at the maximum progress point. To enable trade-off calibration, each deviation can be weighted. Let β_f and β_p represent preference tuning/weighting factors between field-line deviation and maximum progress deviation respectively. There is no optimal selection of these weighting factors, as they are application specific. However, as a reference, $\beta_f > \beta_p$ – for rich path diversities, in order to minimize path deviations, and $\beta_f < \beta_p$ – for applications in which timely delivery is paramount. Figure 12 presents another practical comparison between EFR and FPR's forwarding strategies. As it can be seen, assigning more weight to field line deviation, FPR can yield sequences of relay nodes with minimal deviation from the field lines. Relation 11 can be, consequently, expressed equivalently as follows:

$$sn_k = \Gamma(sn_i, \varphi) \triangleq Argmin_{sn_i \in NB_c} \{\eta(sn_i, sn_c, \varphi)\} \tag{12}$$

We continue now with the evaluation of two important parameters: the maximal progress point coordinate, cf. Figure 11(b), and the field line magnitude limits, cf. Figure 11(a), required for evaluation of $\overline{\Delta}_p$ and $\overline{\Delta}_f$. Subsequently, the FPR forwarding algorithm is being presented.

Maximum Progress Point. Determining the maximum progress point $L_{mpp}(sn_c, \varphi)$ relative to a relay node sn_c and reference field line φ is necessary for evaluation of the progress deviation factor $\overline{\Delta}_p$. The maximum progress point is given by the intersection of the communication disk $\partial(sn_c, R_c)$ of the current relay node sn_c, having a transmission range R_c, with the reference field line φ.

Traditionally, determination of the maximum progress point may be very difficult to be accomplished parametri-

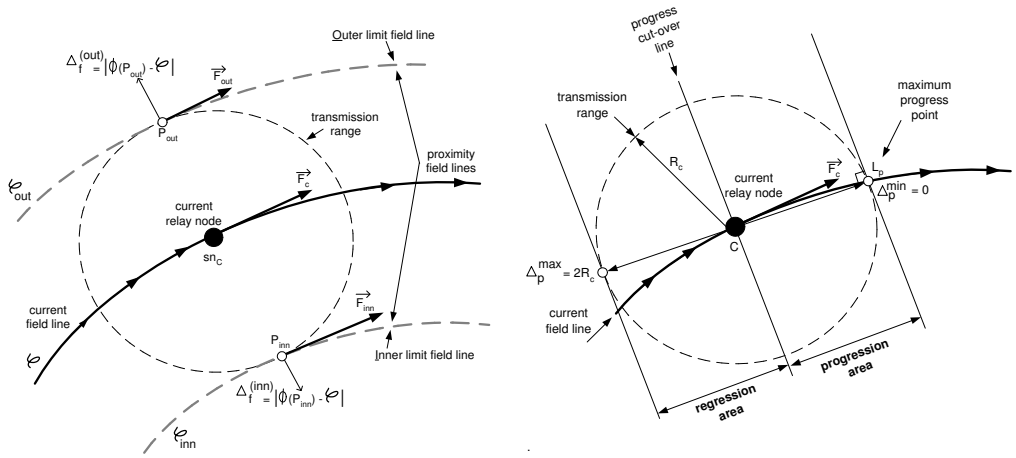

(a) Field Line Magnitude Deviation Limits (b) Forwarding Progress Deviation Limits

Figure 11: Deviation limits

cally, i.e. via solving a complex set of differential equations, and in some cases impossible as the set of differential equations may not have a single solution. From a practical and feasible standpoint, considering the limited computational power sensor nodes posses, we propose an approach that relies on an important property of the electrostatic field and electrostatic field lines. Specifically, the electric field is a continuum surface, and electrostatic field lines do not distinctively exists in the field, they are a mere abstract visual representation that aids describing the electrostatic field intensity and direction of the field at arbitrary locations. However, the "virtual" field lines, when visually represented, they do poses a non-braiding property which is relied upon to build non-braiding routes. To this end, rather than parametrically determine $L_{mpp}(sn_c, \varphi)$, we rely on a numerical solution, which is based on the same concept that underlies the visual representation of the electrostatic field lines in a 2D field, such as a computer screen.

Specifically, we determine $L_{mpp}(sn_c, \varphi)$ by effectively plotting a path-segment of the field line, in memory, by each active relay node, and mapping the plot in the physical field. For this, we use the field line plotting algorithm developed by L. Kirkup [33], which follows the field line path construction mechanism devised initially by [45]. We subsequently refer to this mechanism as the Kirkup-Merrill field line calculation mechanism, or shorthanded as KM-path mechanism.

According to [33], the KM-path mechanism relies on two important field line properties: (1) field line vector is tangent and thus "parallel" to the electrostatic field at the tangential point, and (2) the number of field lines per unit area is proportional to the magnitude of the field at that point. Kirkup acknowledges Merrill [45] to be the first to demonstrate that it is possible to use the first property to calculate the field line path. The main observation is that, considering a field vector $\vec{E}$ evaluated at a certain location (x_c, y_c) represented along the two cartesian coordinates E_x and E_y cf. Figure 13(a), a small displacement D along the field line from the current location x, y can be made under a linear approximation of a field segment of size D, as illustrated in Figure 13(b). The consequence is that, for very small displacements D, the triangles formed by the vectors in Figure 13(a) and 13(b) are similar. Consequently, the displacement Δ_x and Δ_y along the cartesian axes can be computed trigonometrically as:

$$\begin{aligned} \Delta_x &= D\ \cos\theta = \frac{DE_x}{\sqrt{(E_x^2+E_y^2)}} \\ \Delta_y &= D\ \sin\theta = \frac{DE_y}{\sqrt{(E_x^2+E_y^2)}} \end{aligned} \tag{13}$$

Complete end-to-end plot of a electrostatic field line can be carried by applying iteratively the relations 13. For determining $L_{mpp}(\varphi)$, a node needs determining only a small segment of the field line, not the entire field. For this, the iterative process is initiated by the current relay node sn_c located at (x_c, y_c). Figure 14 illustrates the process. The field line segment need not span outside the communication range R_c, hence the iterative process termination criteria can be formalized as:

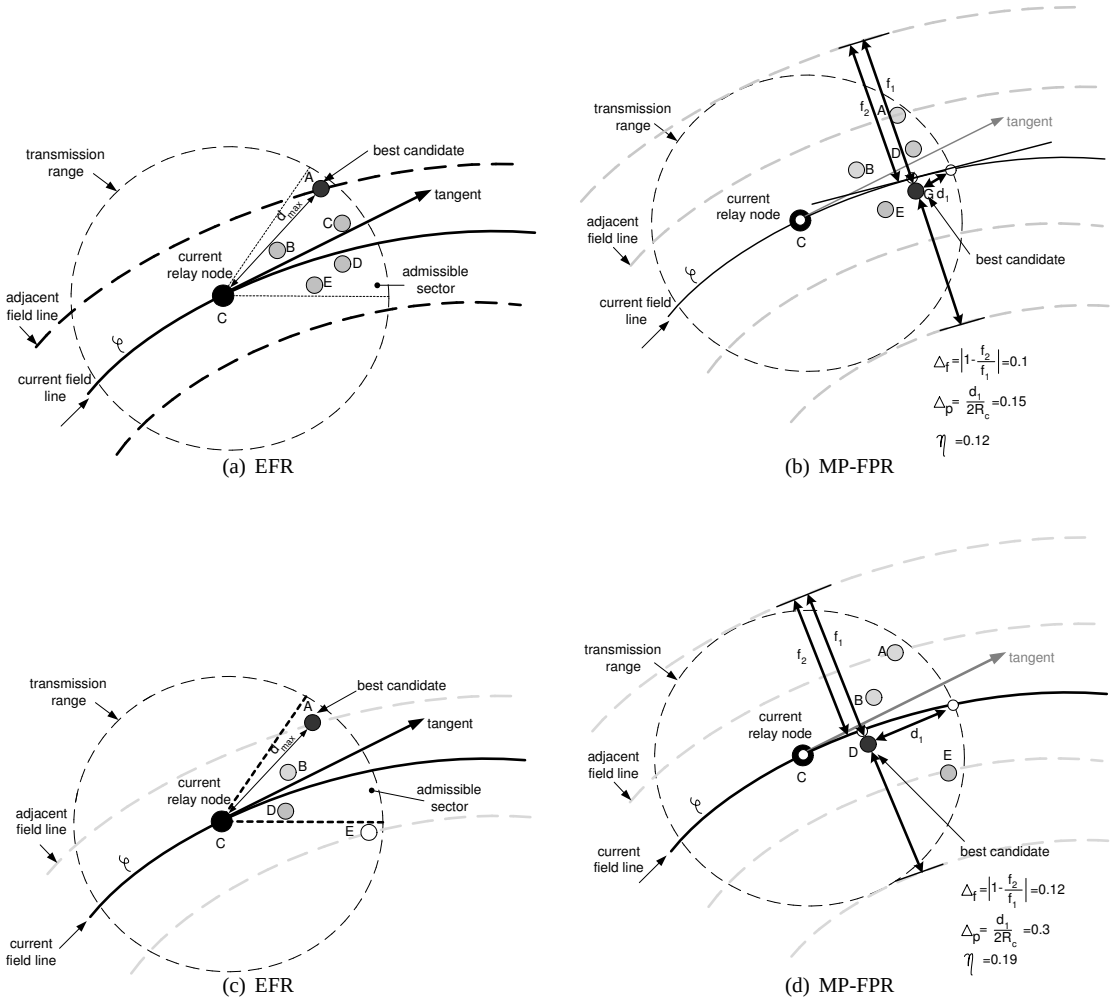

Figure 12: EFR vs FPR forwarding comparison where FPR's weights of $\beta_f = .6$ and $\beta_p = .4$ favor reducing path deviations. Scenario a)-b): nodes A and G are the best candidates according to the EFR and FPR forwarding strategies, respectively. A provides maximum advancement, but yields significant deviation from the reference field line that may cause overload of A via path merging. Scenario c)-d): node D provides least advancement for FPR, increasing hop count, however energy consumption balance is maintained by keeping the relay node close to the reference line φ

$$\|(x_c, y_c), (x_k, y_k)\| \geq R_c \tag{14}$$

where (x_k, y_k) represent the location obtained after k^{th} displacement operation, and $\|(x_c, y_c), (x_k, y_k)\|$ represents the Euclidean distance between the two points. This condition stems from the definition of the maximal progress point, which is defined at the boundary of the communication range, i.e.

$$\|L_{sn_c}, L_{mpp}(sn_c, \varphi)\| = R_c \tag{15}$$

Algorithm 3.1.2 summarizes the steps required to calculate the maximum progress point $L_{mpp}(sn_c, \varphi)$. The algorithm starts with an initial estimate of the maximal progress point, given as the intersection of the communication disk edge $\partial(sn_c, R_c)$ with the segment determined by the tangent at the reference field line φ, cf. Lines 1-4. Iteratively, the tangent segment is rotated clockwise or counter-clockwise in order to obtain closer maximal progress point estimates,

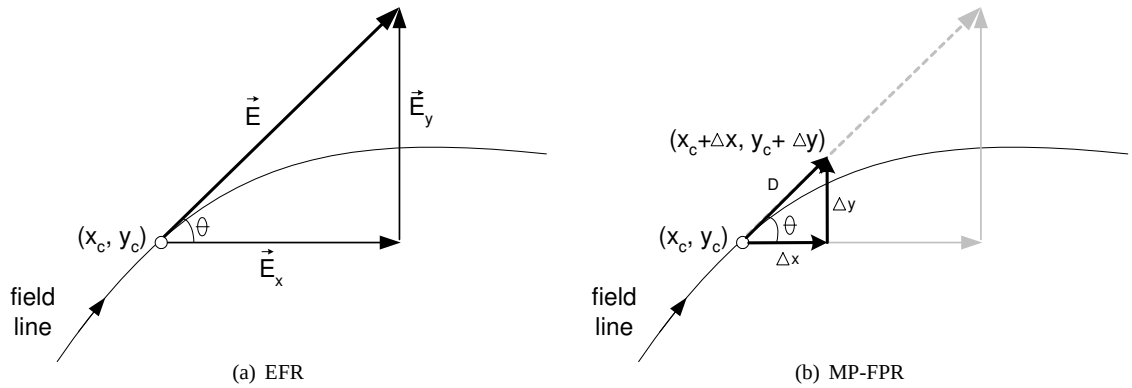

(a) EFR (b) MP-FPR

Figure 13: a) Electrostatic field vector cartesian representation at current node sn_c location, (x_c, y_c); b) Small step D advancement along a linear approximation of the field line

cf. Lines 7-13. Algorithm terminates when a maximal progress point estimate has been determined with a predefined accuracy threshold ε, cf. Line 6. The logarithmical reduction of the rotational amounts dictates the run-time complexity of the algorithm of $O(\lg m)$, where $m \cong \frac{\pi R_c}{\varepsilon}$ represents the rotational resolution required to attain estimates with accuracy ε in the progressive plane cf. Figure 14. In general, larger network size and/or path lengths result in better initial estimates of the maximal progress point, consequently the constant embedded in the run-time complexity is small.

The accuracy of the $L_{mpp}(sn_c, \varphi)$ is given by the size of the field line displacement D, i.e. $L_{mpp}(sn_c, \varphi), (x_k, y_k)\| \leq D$. The runtime performance of the algorithm is approximatively $O(R_c/D)$, i.e. linear with the number of displacements within communication range (assuming linear approximation). As it can be seen, displacement D effectively establishes a tradeoff between accuracy of field line representation and computational overhead. Determining the optimal tradeoff does not make the subject of this work and we consider it a configurable system parameter, however, we note that it may be adjusted depending on the communication range and/or the length of the field lines.

In a sense, Algorithm 3.1.2 can be expanded to determine the entire field line within communication range, not only in the progression field, effectively yielding a distributed variant of KM-path based electrostatic field line determination. Accordingly, each sensor node builds only small parts of a field line, which we refer to as field line *fragments*, with no global representation required. End-to-end routing along a particular field line is enabled by the fact that sensor nodes associated with a particular route contain, collectively, all partitions of a complete electrostatic field line. Figure 15 illustrates the distributed determination and representation of an electrostatic field line in a sensor network.

Field Line Magnitudes Limits.

Normalized orthogonal deviations with respect to the field vector of the reference field line φ can be evaluated by determining the ratio between the Euclidean distance d_i of a particular sensor node sn_i from the reference field line to the maximum deviation space given by the communication range, R_c; specifically, $\Delta_f = \frac{d_i}{R_c}$. Note that this method represents an efficient, yet more precise, deviation measurement than the original definition based on field line indexes c.f. relation 9, since it is evaluated in the close proximity of the maximal progress point and current sensor node sn_c.

This approach relies on the same assumption used for determining the KM-path: field line "arch" between two sampling points $k-1$, k can be linearly approximated if the KM-path field line displacement D is small. Consequently, for a sensor node sn_i, the distance between the node and the field line curve d_i can be approximatively determined by the height of the triangle (L_{k-1}, L_{sn_i}, L_k), where L_{k-1} and L_k represent the two closest sample locations along the field line to L_{sn_i}, where $\{L_{k-1}, L_k\} \subset \widetilde{L_f} = \{L_1, L_2, \ldots, L_{mpp}\}$ represent the set of sample field line locations resulting from execution of Algorithm 3.1.2. We refer to the process of determining L_{k-1}, L_k for a particular candidate relay node sn_i as *field line proximal sample search*, and the respective field line samples L_{k-1}, L_k – proximal field line samples.

Assuming that L_f are being cached locally at sn_c, the proximal field line samples L_{k-1}, L_k can be determined via

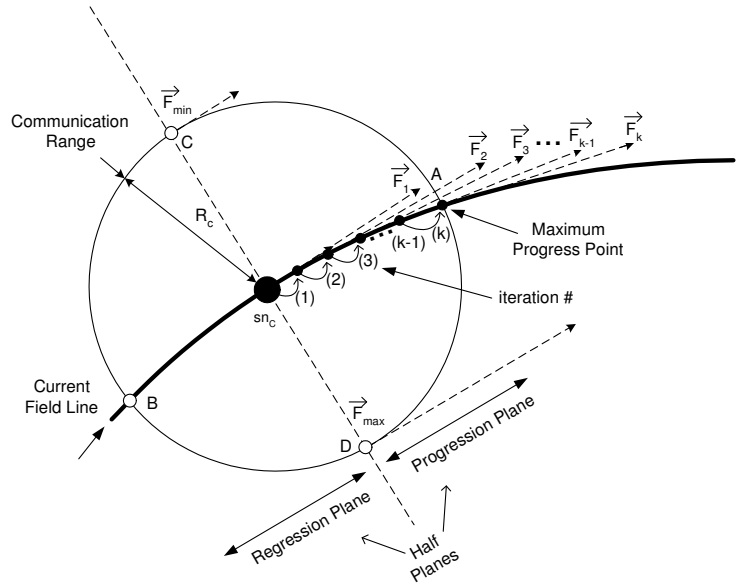

Figure 14: The iterative process for determining the maximum progress point. Given an initial location (x_c, y_c), iteratively perform small displacements (Δ_x, Δ_y) until the entire field line segment delimited by the communication range, in the progression plane, is completely determined.

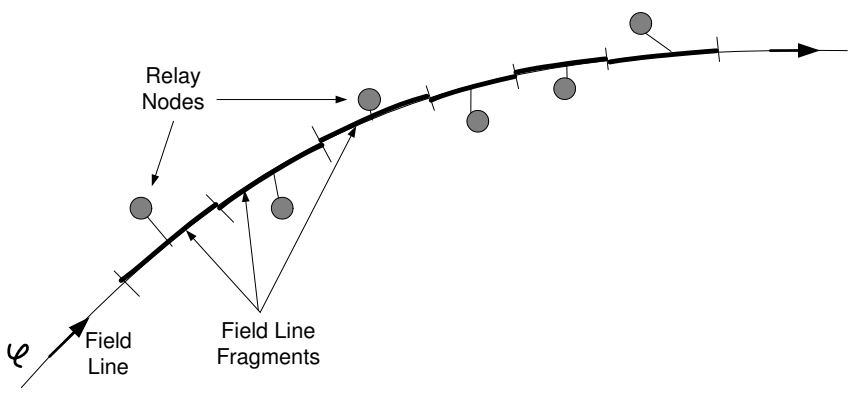

Figure 15: Distributed processing of KM-path. Electrostatic field line fragments are computed, in a completely distributed manner, by the relay nodes associated with a particular field line φ

binary search over $\widetilde{L_f}$. The run time of this process is $O(lg|\widetilde{L_f}|)$, where $|\widetilde{L_f}|$ represents the cardinality of field line sampling set $\widetilde{L_f}$. Figure 16(a) illustrates this process. Subsequently, the height of the triangle trivially by applying a derivation of Heron's formula, and it is given by the following relationship:

$$d_i = \frac{2}{c}\sqrt{s(s-a)(s-b)(s-c)} \tag{16}$$

and, correspondingly, the field line orthogonal deviation:

$$\Delta_f = \frac{2}{cR_c}\sqrt{s(s-a)(s-b)(s-c)} \tag{17}$$

Algorithm 1 Maximum Progress Point Evaluation

Input:
$q_{snk}, \{q_{src}\}$: the sink and sources charges information,
φ: the original field line,
sn_c: the location of the current-relay sensor node,
R_c: the communication range
D: displacement
Output:
$L_{mpp}(\varphi)$ - the maximum progress point w.r.t. to original field line φ
Algorithm:

1: Evaluate field vector $\vec{E}$ at L_{sn_c} using relation 5
2: k = 0
3: $x_k = x_c$
4: $y_k = y_c$
5: **while** $\|(x_c, y_c), (x_k, y_k)\| < R_c$ **do**
6: $\quad k \leftarrow k+1$
7: $\quad$ Determine Δ_x and Δ_y using relation 13
8: $\quad x_k = x_{k-1} + \Delta_x$
9: $\quad y_k = y_{k-1} + \Delta_y$
10: **end while**
11: $L_{mpp}(sn_c, \varphi) \leftarrow (x_k, y_k)$

where:

$$\begin{aligned} a &= \|L_{sn_i}, L_{k-1}\| \\ b &= \|L_{sn_i}, L_k\| \\ c &= \|L_{k-1}, L_k\| \\ s &= \tfrac{a+b+c}{2} \end{aligned} \tag{18}$$

conform notations from Figure 16(b).

Forwarding Algorithm.

The field persistent node selection process is summarized in Algorithm 2, and consists of the necessary steps to perform the evaluation of expression 12. The complexity of the algorithm is $O(n + lgm)$, linear in the number of candidate neighbors $n = |NB_i|$ of a current forwarding node sn_c, and $m = \frac{\pi R_c}{\varepsilon}$, corresponding to Line 1 and Line 5 of the Algorithm. The evaluation of the field line magnitudes limits, as well as the normalized deviations $\overline{\Delta}_f$ and $\overline{\Delta}_p$ can be evaluated in constant time.

There is one important aspect that remains to be addressed. The formalization of the field persistent forwarding has been presented on an assumption that the current relay node residency field line coincides with the reference field line φ. In reality, this need not be the case. To address this problem, we adopt an anchor based mechanism, which enables virtualization of the location of a sensor relay to enable the aforementioned residency assumption, as long as distance between the two locations, real and virtual, is within theoretical communication range. This approach enable a virtual compensation of the path deviation, however, the two different paths, i.e. real and virtual, must remain tightly coupled in order to ensure the communication range restriction throughout the route. These aspects are addressed next.

Path Deviation Compensation.

We formally define a *path* between two distinct sensor nodes as an acyclic sequence of relay nodes $\Upsilon = < sn_1, sn_2, \ldots sn_k >$, such that $\|sn_i, sn_j\| \leq R_c$ for any sub-sequence $< sn_i, sn_j > \subset \Upsilon$, where $\|sn_i, sn_j\|$ represents the Euclidean distance between the two sensor nodes' locations. Under ideal conditions in which a sensor network is infinitely dense (a continuum), given a reference field line φ, the shortest path, in terms of hop-count, associated to the

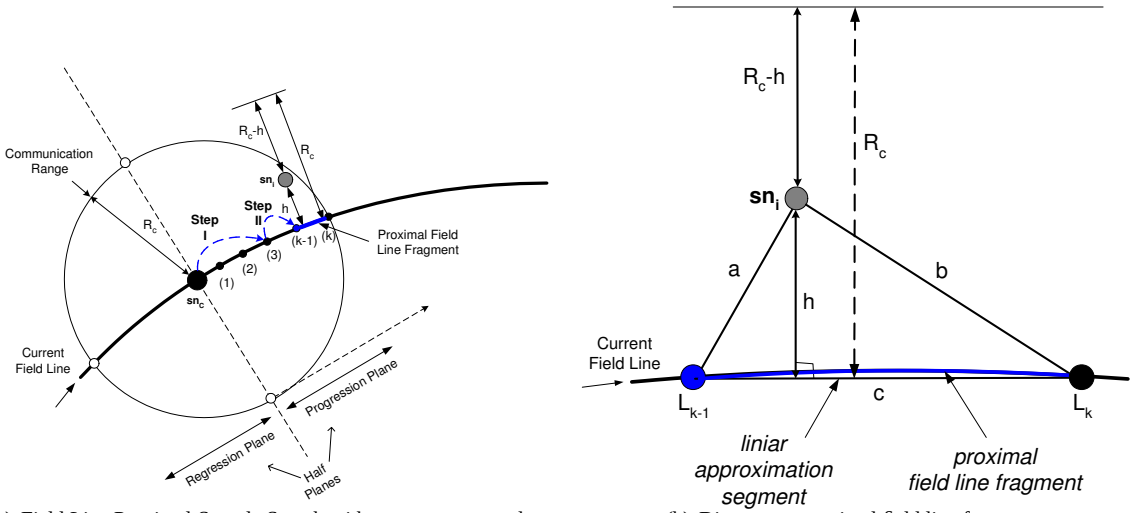

(a) Field Line Proximal Sample Search with respect to sn_c and sn_i

(b) Distance to proximal field line fragment

Figure 16: a) Binary search of proximal field line fragment with respect to candidate relay node sn_i; b) Geometric distance to the proximal field line fragment's linear approximation segment from candidate node sn_i

particular reference field line, effectively consists of a sequence $\overline{\Upsilon}(\varphi) =< \overline{sn_1}, \overline{sn_2}, \ldots \overline{sn_k} >$ of (virtual) sensor nodes all of which are residents on the reference field line, and each of which evenly spaced along the field line at a distance R_c given by the boundary of the communication range, i.e. $\|\overline{sn_i}, \overline{sn_j}\| = R_c$, for any sub-sequence $< \overline{sn_i}, \overline{sn_j} > \subset \overline{\Upsilon}(\varphi)$. The corresponding sequence of 2D coordinates of the sensor nodes on path $\overline{\Upsilon}(\varphi)$, namely $< \overline{L_1}, \overline{L_2}, \ldots, \overline{L_k} >$ represent, in fact, a sequence of maximal progress points along the same reference field line, $< L_{mpp_1}, L_{mpp_2}, \ldots, L_{mpp_k} >$.

Under realistic settings, however, in which sensor network densities are finite, not all of the sensor nodes that form a real path $\Upsilon(\varphi) =< sn_1, sn_2, \ldots sn_k >$ will be residents of the associated reference field line φ. However, it is possible to obtain a mapping from $\Upsilon(\varphi)$ to $\overline{\Upsilon(\varphi)}$ paths, since the forwarding decision in MP-FPR is based on the distributed set of maximal progress points, i.e. $\overline{\Upsilon(\varphi)}$. Accordingly, for each reference electrostatic field line φ between a source and a sink node, two distinct paths are devised: a *virtual* path, $\overline{\Upsilon}(\varphi)$, and a *real* path, $\Upsilon(\varphi)$. The mapping between the two paths must satisfy the following property, whenever possible: for any real relay $sn_i \in \Upsilon(\varphi)$, there exists a virtual anchor $\overline{sn_j} \in \overline{\Upsilon(\varphi)}$ such that $\|sn_i, \overline{sn_j}\| < R_c$. We refer to this property as the *node coupling property*. Under the virtual anchor model, forwarding decisions are made according to an infinite dense network model, however, the actual relay nodes in the real field represent mappings to respective anchors. Equivalently, actual relay nodes sn_i act as "hosts", as they perform the computations and communication tasks associated with a forwarding decision on behalf of a virtual node $\overline{sn_j}$ situated at L_{mpp_j}. Figure 17 illustrates the association of host nodes to virtual nodes.

The overhead of this virtualized routing approach consists of sending one virtual location $L_{mpp_i}(\varphi)$ along with the payload message. Field persistent forwarding is evaluated relative to the current virtual location, rather than current host node. i.e. $L_i \leftarrow L_{mpp_i}(\varphi)$, $1 \leq i \leq n$.

The last remaining challenge is maintaining a tight coupling between $\overline{\Upsilon}(\varphi)$ and $\Upsilon(\varphi)$ paths, i.e. ensure satisfaction of the node coupling property whenever possible. An upper bound on the coupling between the two paths can be quantitatively measured via a restricted, discrete Frechet distance metric, and the goal is to maintain the coupling among the two paths bounded by a finite amount. A quick overview over the Frechet Distance is presented next.

Discrete Frechet Distance Overview

In mathematics, the Frechet distance is a measure of similarity between curves that takes into account the location and ordering of the points along the curves.

Let A and B be two given curves. Then, the *Frechet distance* between A and B is defined as the infimum over all reparametrizations α and β of $[0,1]$ of the maximum over all $t \in [0,1]$ of the distance in S between $A(\alpha(t))$ and $B(\beta(t))$. In mathematical notation, the Frechet distance F(A, B) is:

Algorithm 2 Forwarding Algorithm

Input:
$q_{snk}, \{q_{src}\}$: the sink and sources charges information,
φ: the original field line,
sn_c: the location of the current-relay sensor node,
R_c: the communication range
ε: accuracy parameter
β_f, β_p: the cost function weights for the field line deviation $\overline{\Delta}_f$, respectively progress deviation $\overline{\Delta}_p$ components
Output:
sn_{next} - the identity of the next relay node
Algorithm
1: Determine $L_{mpp}(\varphi)$ using Algorithm 3.1.2
2: Determine φ_{max} and φ_{min}
3: Evaluate $\overline{\Delta}_f$ cf. relation 9
4: Evaluate $\overline{\Delta}_p$ cf. relation 10
5: $sn_{next} = \Gamma(sn_i, \varphi)$, cf. relation 12

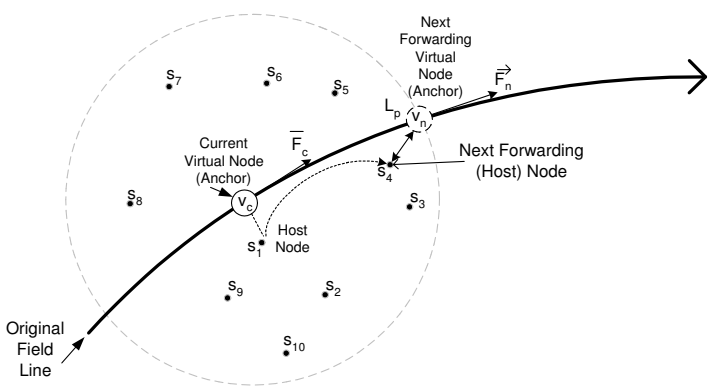

Figure 17: Mapping of virtual nodes to host nodes. Virtual node V_c is hosted by node S_1, whereas the next virtual hop V_n is hosted by node $S_4 \in NB_{S_1}$

$$F(A,B) = \inf_{\alpha,\beta} \max_{t\in[0,1]} \|A(\alpha(t)) - B(\beta(t))\| \tag{19}$$

The Frechet metric takes into account the flow of the two curves because the pairs of points whose distance contributes to the Frechet distance sweep continuously along their respective curves. This makes the Frechet distance a better measure for similarity of curves than alternatives, such as the Hausdorff distance. It is possible for two curves to have small Hausdorff distance but large Frechet distance. If A and B are two curves, the decision problem for the Frechet distance can be expressed as whether $F(A,B) < c$, where c is an arbitrary constant.

The discrete Frechet distance, also called the coupling distance, is an approximation of the Frechet metric for polygonal curves, defined by Either and Mannila [56]. The discrete Frechet distance considers only the distance between vertices of two polygonal representation of curves, without assessment of intermediary points along its segments. This special structure allows the discrete Frechet distance to be computed in polynomial time by an easy dynamic programming algorithm.

Bounded Path Coupling for Minimal Path Deviation.

Because vertices in a real path are uniquely associated to vertices in the virtual path, a restricted version of the discrete Frechet distance is necessary to accurately evaluate an upper bound on the coupling among the two distinct

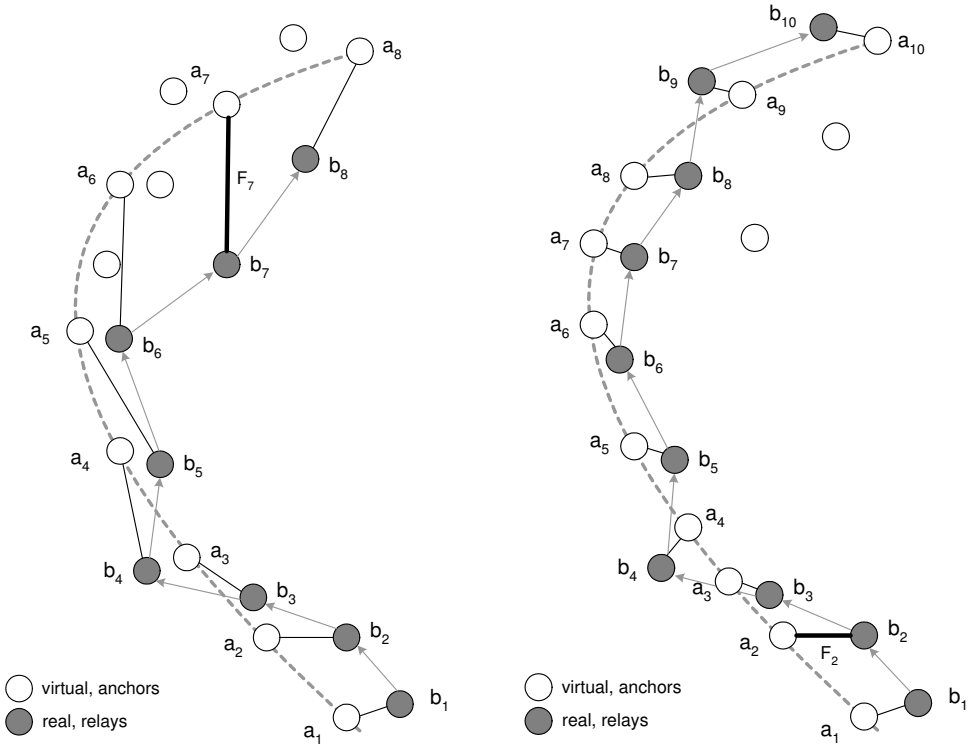

(a) Poor Path Coupling (b) Good Path Coupling

Figure 18: a) Example of a poor path coupling; severe path deviations may develop towards the sink node; F_7 represents the restricted, discrete Frechet distance among the two paths. b) Example of good path coupling, with minimal and consistent path deviations throughout the route; F_2 represents the restricted, discrete Frechet distance in this scenario. It can be observed that $F_2 < F_7$

paths. The restriction reduces the evaluation space to one, in which a vertex k in $\overline{\Upsilon}(\varphi)$ is evaluated against vertex k in $\Upsilon(\varphi)$. Figure 18 illustrates this evaluation for two different paths. As it can be observed, the distance between two consecutive vertices, corresponding to $\overline{\Upsilon}(\varphi)$ and $\Upsilon(\varphi)$, can vary significantly, because: (1) the virtual paths is dictated by the communication range and the curvature of the field line, whereas (2) the real path is dictated by the local distribution of nodes in the vicinity of a host node. Consequently, large Frechet distances correlates to the case in which path coupling is poor, i.e. large deviations exist among the two paths. The goal of this Section is to devise an algorithm that can control the generation of anchor points in a manner in which path coupling is bounded and small.

Let $\overline{d}_{\overline{\Upsilon}(\varphi)} = \frac{1}{n}\sum_{i=2}^{i=n}\left\|\overline{L}_{i-1},\overline{L}_i\right\|$, and $\overline{d}_{\Upsilon(\varphi)} = \frac{1}{n}\sum_{i=2}^{i=n}\|L_{i-1},L_i\|$ represent the average distance between consecutive locations in the two associated paths paths, virtual and real path respectively. Note that, due to the ideal context in which the virtual $\overline{\Upsilon}(\varphi)$ is built, i.e. each subsequent relay sn_{i+1} node is found at the boundary of the communication range R_c of the forwarding node sn_i, then $\overline{d}_{\overline{\Upsilon}(\varphi)} = R_c$. In real conditions, it is expected that $\overline{d}_{\Upsilon(\varphi)} < R_c$, as it is may be the case that forwarding nodes can not be found at the maximum progress point location, however, it is expected that $\overline{d}_{\Upsilon(\varphi)} \to R_c = \overline{d}_{\overline{\Upsilon}(\varphi)}$ as the density of nodes $\rho \to \infty$.

In practice, network densities are finite. Consequently, the coupling distance between $\overline{\Upsilon}(\varphi)$ and $\Upsilon(\varphi)$, i.e. $\left|\overline{d}_{\overline{\Upsilon}(\varphi)} - \overline{d}_{\Upsilon(\varphi)}\right|$ is expected to grow, as a measure of increasing path deviations. This phenomenon is particularly observed towards the end of long paths, in the vicinity of the sink nodes, as illustrated in Figure 18(a). However, such deviations can be controlled and bounded. For this, we evaluate the inter-path coupling at each hop k, i.e. the actual distance between the actual sensor node sn_k located at L_k and the corresponding anchor point at $\overline{L}_k = L_{mpp_k}$, i.e. $\delta^{(k)}_{\overline{\varphi},\varphi} = \|\overline{L}_k, L_k\|$. During a message forwarding step, run-time adjustments to the process by which the anchors are determined are needed in order to maintain the path coupling within predefined limits, equivalently, maintain the

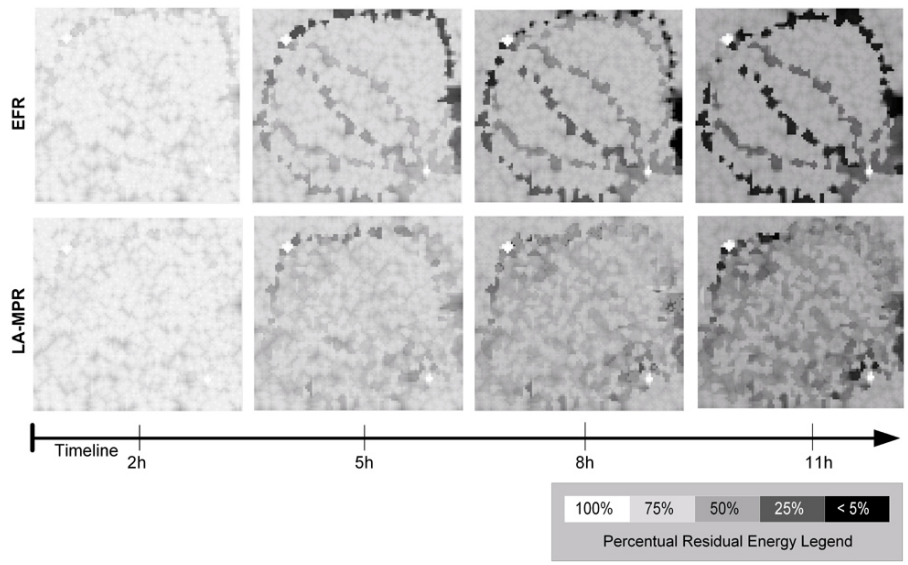

(a) using EFR

Figure 19: Energy Depletion Maps

following path coupling invariant:

$$\delta^{(k)}_{\overline{\varphi},\varphi} < \psi \tag{20}$$

where $0 < \psi < R_c$.

Maintaining this invariant will ensure that the Frechet distance between the end-to-end real and virtual paths is also bounded:

$$F(\overline{\Upsilon}(\varphi), \Upsilon(\varphi)) < \psi \tag{21}$$

The sequence of anchors $\overline{\Upsilon}(\varphi)$ along a reference field line φ is effectively dictated by two factors: distribution of electrostatic charges, and the communication range R_c. Recall that each anchor is dictated by the maximum progress point evaluated via Algorithm 3.1.2. One can control the placement of a certain anchor point by effectively modifying the communication range, namely using a virtual range parameter R'_c such that $R'_c \leq R_c$. This approach can effectively reduce $\overline{d}_{\overline{\Upsilon}(\varphi)} = R'_c \leq R_c$. Thus, it is possible to control the execution of Algorithm 3.1.2 such that $\delta^{(k)}_{\overline{\varphi},\varphi} < R_c$, as it will be shown next.

Algorithm 3 represents an adaptation of the forwarding Algorithm 2 for arbitrarily dense networks that takes into consideration the specifics of the anchor based forwarding and inter-path coupling issues to ensure minimal path deviation and accurate field-line forwarding. The adaptation is performed in the loop between lines 4 and 11, and the invariant in relationship 20 is ensured via the verification at line 11. The evaluation of the algorithm is made relative to the current virtual location $L_{cur}(\varphi)$, initialized at line 2, and propagation of the maximal progress point $L_{mpp}(\varphi)$ for the next iteration is ensured in Line 12.

We conclude this Section with the following observation. Analogous to EFR [41, 31], the MP-FPR approach proposed here is an instance of the trajectory-based forwarding (TBF) [42] paradigm. To specify a given trajectory, the source selects an *initial outgoing angle* (cf. φ in Figure 4(a)), which the relay-nodes carry over as part of the transmission-packet. This is what enables the source to implement different policies of *alternating* among routes: e.g., by discretizing the values of $\varphi \in [0, 2\pi]$, the family of possible routes can be indexed, and a bound can be placed on their total number. Clearly, this entails that some nodes' locations may not belong to an actual route, however, in such cases (as suggested in the original work [42]) the nodes will be considered to belong to the closest route.

Algorithm 3 Bounded Coupling Field Persistent Forwarding Algorithm

Input:
$q_{snk}, \{q_{src}\}$: the sink and sources charges information,
φ: the original field line,
sn_c: the location of the current-relay sensor node,
R_c: the communication range
ε: accuracy parameter
ψ: maximum admissible path coupling value
ς: communication range regression rate
β_f, β_p: the cost function weights for the field line deviation
$\overline{\Delta}_f$, respectively progress deviation
$\overline{\Delta}_p$ components
$L_{mpp}(\varphi)$, the next virtual relay coordinates
Output:
sn_{next} - the identity of the next relay node
Algorithm:

```
R* ← R
L_cur(φ) ← L_mpp(φ)
repeat
    Determine L_mpp(φ) using Algorithm 3.1.2 with communication range R* and L_cur(φ)
    Evaluate Δ̄_f cf. relation 9
    Evaluate Δ̄_p cf. relation 10
    Determine sn_next by applying relation 12
    Evaluate deviation distance δ = ||L_mpp(φ), L_sn_next||
    R* ← ς R.
until δ ≤ ψ
Embed L_mpp(φ) in the forwarding message
Forward message to sn_next.
```

3.2 Boundary Effects and Method of Images

Some studies have proposed solutions to this problem [31, 52], but these methods yield complicated solutions, or even elude closed-form solutions.

Recall that path merging of initially-different routes can also happen at the geographic boundary of a given network. The so-called boundary condition problem has been solved in [31, 52] via partial differential equations, however, such solution is clearly not practical for WSN settings. Instead, the method adopted herein is based on a well known physical heuristic, (*method of images*), within the same electrostatic framework, to achieve resolve the boundary problems in a simpler and distributed manner.

Let ∂R be the boundary of the deployment region. The goal is to reduce the severity of the path merging effects near the boundary. Assuming that a charge q_1 is located at a distance d from the boundary (cf. Figure 20(a)). Finding a potential ϕ such that $\nabla_v \phi = 0$ for $\mathbf{r} \in \partial R$ will create a zero-potential effect on the boundary, thereby guiding the field lines, and associated paths, away from its border. The method of images suggests to place an additional, virtual charge q_2 at position $-d$ from the boundary segment under consideration. For a given point on the boundary $\mathbf{r} \in \partial R$, we obtain:

$$\phi(\mathbf{r}) = \frac{1}{4\pi\varepsilon_0}\left(\frac{q_1}{|d|} + \frac{q_2}{|d|}\right) \tag{22}$$

and derive $\nabla_v \phi(\mathbf{r}) = 0$ for $\mathbf{r} \in \partial R$.
Knowing the geographical limits of the network (by either pre-loading it or executing an appropriate algorithm [13]),

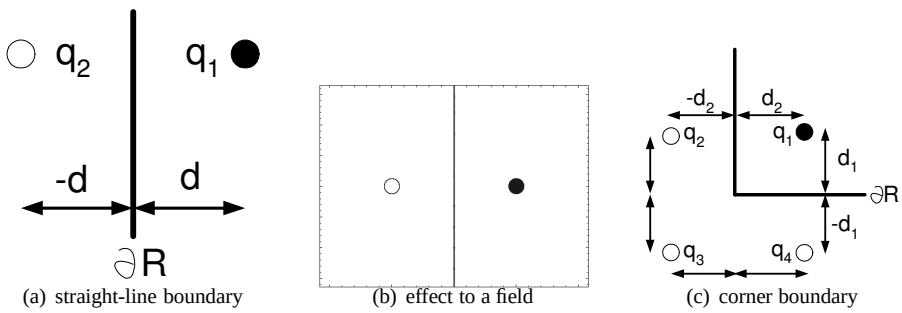

(a) straight-line boundary (b) effect to a field (c) corner boundary

Figure 20: Method of Images: (a) A virtual charge q_2 and a zero potential at ∂R. (b) Decreasing the boundary-paths merging. (c) 3 virtual charges near corners.

each relay node can decide *locally* whether to apply the method of images or not. If a given node is close to the border, it will include the virtual image charges in the calculation of its field vector. In the case a particular node is close to the corner of the WSN boundary, more than one virtual charges may be needed – e.g., 3 image charges are utilized for the corner in Figure 20(c). We note that the method of images leans on a uniqueness theorem for the Laplace equation, and can be applied to sufficiently regular boundaries.

3.3 Multi-Pole (MP) Protocol for Charge and Route Management in MP-FPR

One of the key advantages of multipole electrostatic routing is its capability to reduce MAC collisions by forming mutually exclusive routing areas for each source (cf. Figure 8(b)). To realize such mutually exclusive areas, each source needs to have an up-to-date information about the existing charges (sources) in the network. A dissemination mechanism was suggested in [31], in which sink and source nodes advertise their locations and respective charges by flooding. This may be a sound choice, assuming that the WSN is dense and the nodes' locations are uniformly distributed, since a significant fraction of sensor nodes can be expected to participate in relaying duties. However, when path-merging occur, the flooding-based dissemination incurs costs that outweigh the benefits. To alleviate the drawbacks of flooding-based dissemination, in this section we present a light-weight, non-flooding protocol for the maintenance of electrostatic multipole fields.

The MP-FPR protocol consists of three main protocol components:

- Query Dissemination and Charge Allocation
- Route Establishment
- Data Forwarding

Also, it is important to note that MP-FPR relies, in fact, on two distinct forwarding mechanisms. First, it relies the electrostatic field line forwarding (EFL) for all heavy and long terms stream delivery, such as user payload information from the source to the sink node. Specifically, EFL consist of all the mechanisms discussed in Section 3.1 and 3.2, such as the accurate field line forwarding and method of images respectivelly. For all other lightweight control messages and related tasks, such as query dissemination, charge and part of the route establishment tasks, MP-FPR partly relies on greedy shortest geographic path (SGP) routing mechanism similar to BVR [18], where packets are sent via a geographically shortest path towards a known physical destination, for the following reason: it does not require prior route testing or establishment, which is ideal for delivery of single-instance messages, such as dissemination of QUERY messages, or short-lived streams, such as acknowledgment messages, which result in improvements in terms of timely completion of control-related tasks, with corresponding reduced energy consumption.

The detailed protocol behavior and interplay of sink and source nodes in our Multi Pole Field Persistent Routing protocol (MP-FPR) is shown in Algorithms 4 and 5. In sequel we provide an overview of each protocol component and the mapping of protocol related tasks to these algorithms, outlining the types and content of the main messages

Table 1: MP-FPR Messages

Type	Functionality	Protocol Phase	Forwarding	Fields of Interest
QUERY	Query Specification Wrapper	Query Dissemination and Charge Allocation	SGP	L_{src}, C_e, N_r,
UPDATE	Charge Information Update	Query Dissemination and Charge Allocation	SGP	L_{src}, C_e
RREQ	Route Request (Probe)	Route Establishment	EFL	L_{src}, C_e, r_i, t_{sent}
ACK	Route Acknowledgment	Route Establishment	SGP	L_{src}, r_i
DATA	User Data-Payload Wrapper	Data Forwarding	EFL	r_i, $Data$

utilized in each of the three protocol components. A summary of these messages is presented in Table 1.

Query dissemination and charge allocation: This protocol component consists of messages generated by the sink and has several goals. First is to forward the user query towards the source and is achieved through a QUERY message sent by the sink with SGP forwarding towards L_{src} – the location within the area where data relevant to the query should be collected from. A sensor node which is geographically closest to L_{src} will assume the role of the source for the given QUERY message, and initiate its processing. Second goal is to disseminate electrostatic charges information, which consists of a set of (location, magnitude and expiration) information associated with each routing end-point, i.e. source or sink node, in the network. For example, if there are m source nodes relaying data-streams to a common sink, the QUERY message contains a set $C_e = \{e_{snk}\} \cup \{e_i | i \in \overline{1,m}\}$ of electrostatic charges [6]. The sink node keeps active sources informed about joining sources via $UPDATE$ messages (cf. Alg. 4, lines 5-7). Upon reception of an $UPDATE$ message, an active source updates its knowledge about other source nodes, sets its active routes to pending, and re-runs the route discovery due to possible changes in the routing behavior of intermediate nodes (cf. Alg. 5, lines 15-23). Third goal is to limit the number of alternative paths to be built in order to correspondingly bound the duration of the route establishment protocol component. We refer to this limit as the *path diversity quota*, and it can be either user specified or system predefined. Path diversity quota is controlled via a numerical parameter $N_r = |S_f|$ embedded in the body of the QUERY message.

The sink node initiates and is in charge for the completion of the query dissemination and charge allocation. Algorithm 4 summarizes all the steps required by the sink to complete this task. It is important to note that the sink node keeps track of all active sources (and their charges) in an appropriate data structure, as illustrated with the update in line 8 of Algorithm 4. The sink unicasts the location of the new source (src') and the assigned charge to the active sources (lines 5-7), and the $QUERY$ message to the new joining source node src' (lines 8-9). Upon reception of a $QUERY$ message, the joining source node resets its state, parses the user query, and starts the route discovery, as specified in lines 3-5, in Algorithm 5.

Whenever a new data source is added to the existing set of source-nodes, a new corresponding charge is added to the virtual electrostatic field. The charge information is being updated at each of the source nodes via an UPDATE message. For example, if there were m different sources in the network, excluding the newest activated one by the last QUERY message, then m UPDATE messages are sent via the SGP forwarding mechanism to each of the m existing source nodes. Upon receival of an UDPATE, route establishing process is re-initiated by the source nodes in order to establish new families of routes that are consistent with the new charge distribution.

Route establishment: Initiated upon receiving a QUERY or UPDATE message at a source node, the *route establishment* is a two-phase, request-acknowledgment process. During the *requesting phase*, the source node selects outgoing angles for the specified path diversity quota information N_r, and transmits a set of corresponding RREQ messages along *distinct* electrostatic field lines towards the sink (cf. Alg. 5, lines 6-10). A RREQ message carries a list of network's current charges C_e as well as the field line index (equivalently route index) $r_i \in S_f$ identifying the field line a specific RREQ message is to be sent along. To amortize the associated transmission cost of the charges, this information is sent only once along along RREQ messages, and cached locally by the route's relay nodes; subsequent DATA messages will not carry them. The source node will also incorporate its actual location information L_{src} in the RREQ message such that sink's maintains a more accurate representation of the actual sources. Note that the actual source's location may not coincide with the user-specified location within the QUERY message due to finite coverage of the deployment area. A timestamp t_{sent} is also included in the RREQ message to assist in determining the quality

[6] In analogy to Coulomb's Law [30], the electric charge assigned to a source is reciprocally proportional to the square of the relative distance between the sink and the source. The charge of the sink is the inverse-sum of the all the charges of the individual sources.

Algorithm 4 Sink behavior in MP-FPR routing protocol

Input
$snk \in \mathbb{R}^2$: position of sink node, $L \subset \mathbb{R}^2 \times \mathbb{R} \times \mathbb{R}$: (position, charge, duration) of active sources
$src_i, src' \in \mathbb{R}^2$: geographic positions, $q \in \mathbb{R}$: electric charge, $t \in \mathbb{R}$: duration time, φ_i: route identifier
Algorithm:

1: **loop**
2: **if** query injected **then**
3: $src', t, \varphi' \leftarrow parse(userQuery)$
4: $q \leftarrow createCharge(src', snk)$
5: **for all** active sources src_i **do**
6: $sendToNet(UPDATE(src_i, snk, (src', q, t))$
7: **end for**
8: $L \leftarrow L \cup (src', q, t)$
9: $sendToNet(QUERY(src', snk, userQuery, \varphi', L))$
10: **else if** message received **then**
11: **if** $type(message) == RREQ$ **then**
12: $src_i, varphi_i \leftarrow parse(message)$
13: $sendToNet(ACK(src_i, snk, varphi_i))$
14: **else if** $type(message) == DATA$ **then**
15: extract sensor readings and present to user
16: **end if**
17: **end if**
18: **end loop**

(e.g. latency) of a specific route. We assume that nodes have loosely synchronized clocks [49].

If, upon the receival of a RREQ message, it is determined that RREQ's route exhibited an admissible latency, the route is acknowledged, during the *acknowledgment phase*, by sending back a corresponding ACK message to the specific source (cf. Alg. 5, lines 11-14). The route index r_i for the route that it acknowledges is included in the ACK message. Note that ACK messages are sent back via the SGP mechanism towards the actual location of the source L_{src}, and not via EFL mechanism the corresponding RREQ message was sent[7]. Every acknowledged route is added to a source-maintained set of acknowledged routes $S_f^{ack} \subseteq S_f$, i.e., a pool of routes that are available for data forwarding.

Data forwarding: The DATA messages pertaining to a data-stream as a result of query processing are forwarded back to the sink node as soon as a source has successfully discovered valid routing paths. DATA messages, which contain user specified information as payload, are forwarded in an alternating manner among the individual routes r_i from the set of acknowledged routes S_f^{ack}, via the EFL mechanism. The source node adjusts the flow rates per route based on the electrostatic field (packets are sent proportionally to the magnitude of the field, as suggested in [31]) (cf. Alg. 5, lines 24-29). Upon receival, the sink node extracts the message payload and returns it to the user application (cf. Alg. 4, lines 14-16).

3.4 QoS-Control Framework Based on Virtual Electrostatic Charges

In this Section we present a mechanism that complements MP-FPR protocol's functionality for ensuring certain user-facing performance guarantees. Field persistent routing and method of images methodologies target primarily network-oriented performances, such as network's operational lifetime via advanced workload balancing techniques. However, one needs also take into consideration the user-facing performance requirements and tolerances, to achieve a feasible balance.

There are two important user-facing performance indicators of interest from a routing perspective: (1) *reliability* and (2) *timeliness* of the data-stream delivery. The former concerns the fraction of the data-stream that was success-

[7]This is to prevent local-minima or other factors to affect the deliverability of the ACK message, thus increasing path diversity

Algorithm 5 Source behavior in MP-FPR routing protocol

Input:
$src, snk \in \mathbb{R}^2$: geographic position, $L \subset \mathbb{R}^2 \times \mathbb{R} \times \mathbb{R}$: (position, charge, duration) of known sources, $R \subset \mathbb{N}$: acknowledged routes, $P \subset \mathbb{N}$: pending routes
$p \in \mathbb{R}^2$: geographic positions, $q \in \mathbb{R}$: electric charge, $t \in \mathbb{R}$: duration time, $\varphi \in \mathbb{R}$: route identifier, $n \in \mathbb{N}$: maximum number of routes
Algorithm:

```
loop
    if message received then
        if type(message) == QUERY then
            L, n, snk ← parse(message)
            P, R ← ∅
            for 1 ≤ i ≤ n do
                φ_i ← 2π·i / n
                P ← P ∪ φ_i
                sendToNet(RREQ(snk, src, φ_i, L))
            end for
        else if type(message) == ACK then
            φ ← parse(message)
            R ← φ
            P ← P \ φ
        else if type(message) == UPDATE then
            (p, q, t) ← parse(message)
            L ← L ∪ (p, q, t)
            for all φ_i ∈ R do
                P ← P ∪ φ_i
                R ← R \ φ_i
                sendToNet(RREQ(snk, src, φ_i, L))
            end for
        end if
    else if sensor reading d available then
        if R ≠ ∅ then
            φ_init ← selectRoute(R)
            sendToNet(DATA(snk, src, φ_init, L, d))
        end if
    end if
end loop
```

fully delivered to the user, while the latter concerns the end-to-end packet delivery latency of the data-packets within the stream. MP-FPR relies on a rich family of paths, each of which used in alternation, as a load-balancing mechanism. The satisfiability of the first performance indicator is consequently trivial: MP-FPR can be easily adapted for alternating subsets of paths, rather than single paths at a time, for delivering copies of a data-packet, as a standard mechanism for improving deliverability performance, therefore we do not pursue this topic further. The *timeliness* of the data-stream delivery is, however, particularly challenging to achieve without directly affecting the workload balancing provisions that trivial route QoS control methodologies based on route suppression (illustrated in Figure 21(a)) may yield, especially considering the lifetime-critical regions in the immediate vicinity of source and sink nodes. We thoroughly analyze the timeliness aspect in sequel.

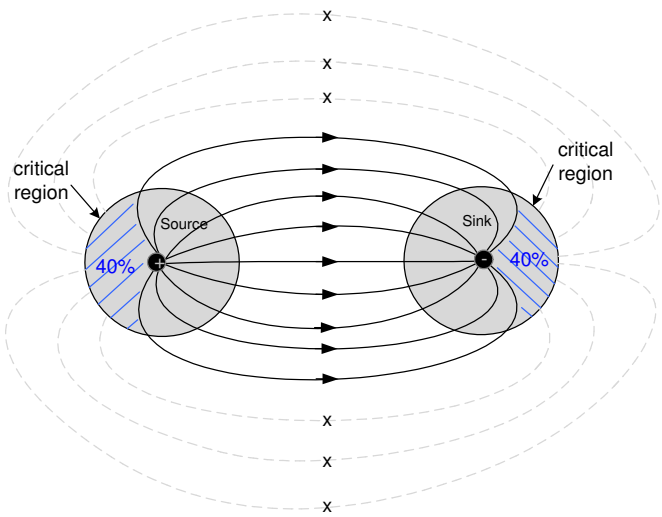

(a) Route Suppression Model

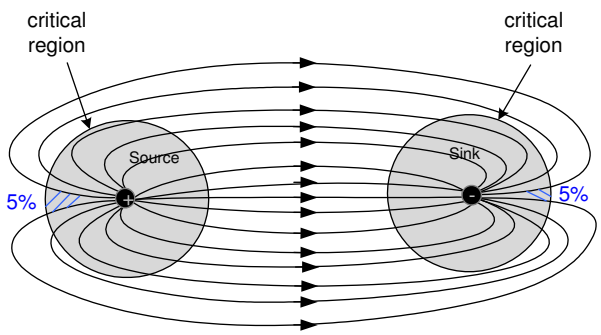

(b) Route Constraining Model

Figure 21: a) Route suppression model for routes QoS control: lengthy routes are discarded from the overall family of routes; the utilization of the relay nodes in the immediate vicinity of source and sink nodes is subsequently affected b) Route constraining model: constrain routes to be built within a smaller allowable routing field, in order to continue to harness the electrostatic field based routing benefits with reduced path diversity impact

3.4.1 End-To-End Packet Delivery Latency Components

Let T_{f_i} denote the amount of time a message spends within a given relay node sn_i. We refer to T_{f_i} as the packet *forwarding* time spent within an arbitrary host node sn_i. The forwarding time accounts for the queuing time T_{q_i}, processing time T_{p_i} and outbound communication time T_{c_i}:

$$T_{f_i} = T_{p_i} + T_{q_i} + T_{c_i} \tag{23}$$

Assuming a path $\Upsilon =< sn_1, sn_2, \ldots, sn_k >$ represented as an ordered sequence of k sensor nodes, then the end-to-end average packet delivery latency T_Υ represents the sum of the packet forwarding times within each relay node, specifically:

$$T_\Upsilon = \sum_{i=1}^{k} T_{f_i} = \sum_{i=1}^{k} (T_{p_i} + T_{q_i} + T_{c_i}) \tag{24}$$

or, alternatively:

$$\overline{T}_{\Upsilon} = k \cdot \overline{T}_f = k \cdot (\overline{T}_p + \overline{T}_q + \overline{T}_c) \tag{25}$$

where $\overline{T}_p$, $\overline{T}_q$, and $\overline{T}_c$ represent the *average* processing, queuing and communication time allocated for forwarding one data-message, under nominal conditions.

In this article we take a holistic approach: we aim at bounding the end-to-end packet delivery latency $\overline{T}_{\Upsilon}$ by controlling the length of the routes $|\Upsilon|$, specifically bounding the length of the longest admissible route.

3.4.2 Real Charges vs. Virtual Charges

The physical path and the length of the electrostatic field lines are entirely determined by the distribution of electrostatic charges in the network. For routing purposes, it is not necessary, and possibly unfeasible, to devise a methodology to enable precise length-control of each route within the family of field lines. It suffices, however, to devise a set of upper and lower bounds on the expected lengths of the electrostatic field lines, and devise a methodology to guarantee that the length of the electrostatic field lines within a given family of field lines comply with the projected bounds. Let sn_{src} and sn_{snk} devise the two end-points of a family of routes. The corresponding charges C_{src} and C_{snk} determine a family of electrostatic field lines S_{φ}, i.e. a set of field lines that have a common source charge and a common sink charge. Let $LL_{S_{\varphi}}$ and $LU_{S_{\varphi}}$ denote the lower and respectively upper bound on the lengths of electrostatic field lines within a family S_{φ}.

Recall that MP-FPR relies on a one-to-one mapping of the set of electrostatic charges to the set of source and sink nodes in the network. Considering that the distance along a field line is evaluated in the Euclidean space, the length of the shortest field line is given by the shortest distance between a pair of source and sink charges. At the other extreme, it is known that the electric field is infinite, therefore some of the field lines are infinitely long. Let, if L_{src} and L_{snk} represent the corresponding locations of the source and sink node (and associated charges). Formally, electrostatic field lines between two point charges are natively bounded by:

$$\begin{cases} LU_{S_{\varphi}} = \infty \\ LL_{S_{\varphi}} = \|L_{src}, L_{snk}\| \end{cases} \tag{26}$$

It is important to note that the lower-bound cannot be improved and it is limited by the physical domain. The upper bound, however, can be reduced if the bijective model is relaxed and a surjective mapping is adopted instead. In the latter mapping model, more than one charge can be associated with each of the source and sink nodes. A second relaxation that needs to be made is that some of the additional charges need not physically coincide with either the source/sink nodes. In this context, we distinguish two categories of charges: *real charges* and *virtual charges*. The real charges represent the set of charges that collocate with the existing source and sink nodes, whereas the virtual charges can be understood as satellite charges, i.e. associated with a particular node, but not sharing the same location. Figure 22 illustrates the distinction and placement of real and virtual charges in the physical domain. The main idea consists of associating the bounds in expression 26 with the virtual charges' field lines, while enabling tighter bounds for the real charges. This mechanism is explained next.

For convenience, given the specifics of the virtual charges, we represent their locations relative to their corresponding real charges in a polar coordinate system, where the real charges represent the origin of each coordinate system, as illustrated in Figure 23.

3.4.3 Electrostatic Field Constrain with Virtual Charges

In this Section we rely, one more time, on the disjointness property of electrostatic field lines. Specifically, we exploit the fact that distinct families of field lines do not intersect in the physical domain, as illustrated in Figure 24(a). Two adjacent positive charges effectively creates a partitioning of the field plane in two sub-planes, with the property that field lines originating at one positive charge will be constrained by the sub-plane field in which that particular charge resides. Moreover, the field lines originating in one sub-plane will never cross the imaginary field partition boundary.

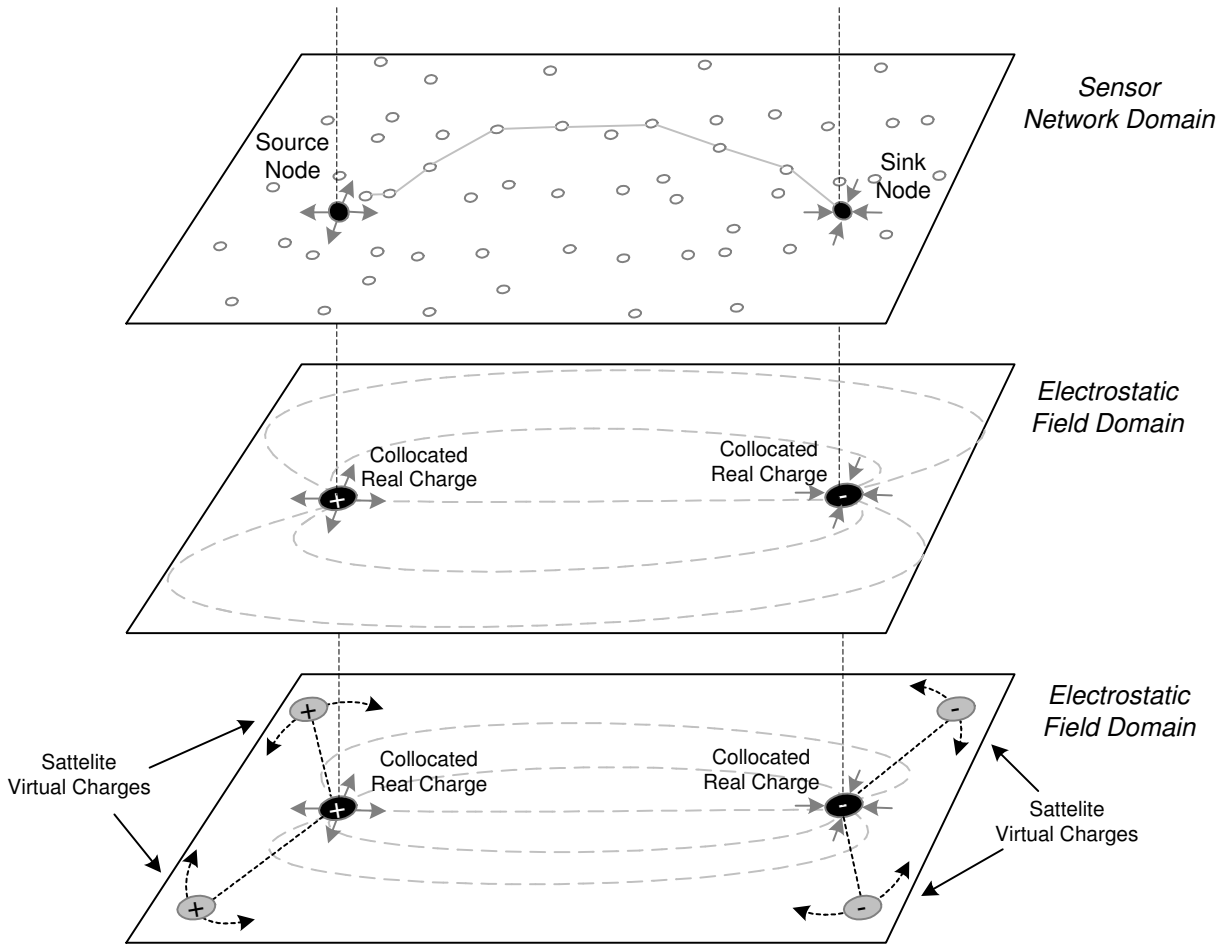

Figure 22: Mapping of real and virtual electrostatic charges to source/sink nodes

Figure 24(b) illustrates the field-plane partitioning effect. Assuming that the positive charges have equal magnitude, then the field line border is at mid-distance between the two positive charges. A snapshot of the real electrostatic field captured in a simulated environment is illustrated in Figure 24(c). We subsequently refer to this effect as the *electrostatic field partitioning*.

The role of the virtual charges is to create such field partitions in a controlled manner. Thus, it is possible to create a closed sub-region in the field that fully constraints the path of a family of field lines via a small set of field partitions. We refer to this sub-region as the *bounding sub-field*, and to the perimeter of the sub-region as the *bounding box*. Figure 25 illustrates the bounding sub-field obtained with a minimum of 4 field partitions via 4 virtual charges. For simplicity, and without loss of generality, we assume that charges have equal magnitudes.

3.4.4 Tight Upper Bounds via Bounding Box and Bounding Sub-Field

The upper bound LU_{S_φ} is dictated by the perimeter of the bounding box of the sub-field, which can be evaluated trigonometrically. In this section we devise the upper bound under the following simplifying assumptions: (1) the magnitude of the virtual charges equals the magnitude of the associated real charges, i.e. $|V_1^+| = |V_2^+| = |R^+|$ and $|V_1^-| = |V_2^-| = |R^-|$ (cf. notations in Figure 25), (2) the radial distance between virtual and corresponding virtual charges is equal, i.e. considering the Euclidean distance between charges, $\|L_{V_1^+}, L_{R^+}\| = \|L_{V_2^+}, L_{R^+}\| = 2r$ and

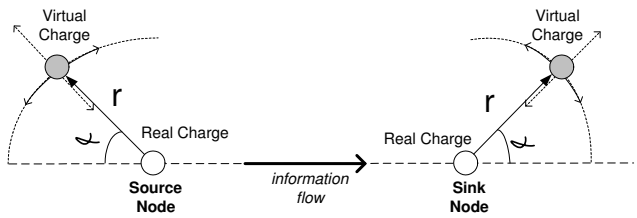

Figure 23: Polar representation of virtual charges relative to origins dictated by the source and sink nodes' associated real electrostatic charges' locations; angular representation is relative to source-sink axis; the two coordinate systems are mirrored

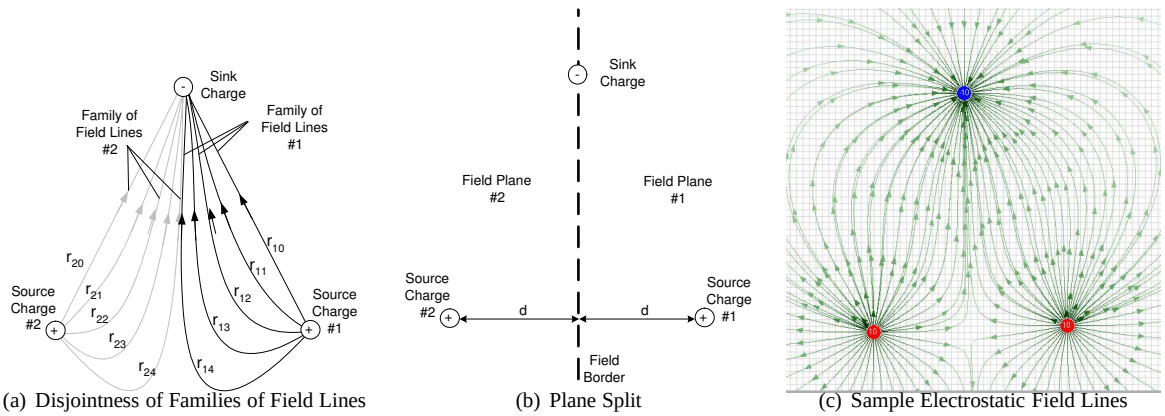

(a) Disjointness of Families of Field Lines (b) Plane Split (c) Sample Electrostatic Field Lines

Figure 24: a) Disjointness of two distinct families of field lines; field lines pertaining to the two illustrated families do not intersect; b) Conceptual division of the electrostatic field as a result of two positive electrostatic charges; the field border is at mid-distance between the positive charges if charges have equal magnitudes; c) Snapshot of corresponding electrostatic field in simulator

$\|L_{V_1^-}, L_{R^-}\| = \|L_{V_2^-}, L_{R^-}\| = 2r$, for some constant r, where $L_{V_1^+}$, $L_{V_2^+}$, L_{R^+}, $L_{V_1^-}$, $L_{V_2^-}$, L_{R^-} represents the coordinates of the respective charges from Figure 25, and (3) charge angular placement is symmetric, each virtual charge being placed at an angle α from its respective coordinate system w.r.t. to the conventions established in Figure 23. Figure 26 illustrates the bounding sub-field that conforms to these simplifying assumptions.

Consequently, the longest field line that can be created within a bounding sub-field is smaller than or equal with half of the perimeter of the corresponding bounding box, plus the distance from each real charge to the closest vertex of the subfield. For example, according to notations in Figure 26, the upper bound on the length of the field lines can be reduced to:

$$LU_{S_\varphi} = 2L_e \cdot = 2(L_x + L_y + L_z + L_d) \tag{27}$$

where $L_e = L_x + L_y + L_z$ represents the the length of an edge of the field bounding box, while L_d the distance to the closest vertex on the bounding box. Applying basic trigonometry:

$$\begin{cases} L_x = r\tan\alpha \\ L_y = r\cot\alpha \\ L_z = \frac{L}{2\sin\alpha} \\ L_d = r\cos\alpha \end{cases} \tag{28}$$

where $L = \|R^+, R^-\| = \|L_{src}, L_{snk}\|$ represents the Euclidean distance between the source and sink node.

Consequently, the new, tighter bounds on the lengths of the electrostatic field lines are given by:

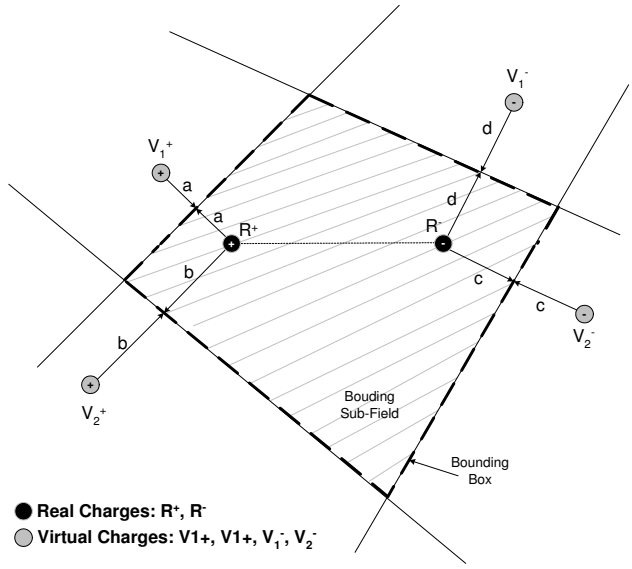

Figure 25: Partitioning of the field plane can yield a closed region that the field lines between the two real charges are contained within.

$$\begin{cases} LU_{S_\varphi} = \|L_{src}, L_{snk}\| \frac{1}{\sin\alpha} + \frac{2r}{\sin\alpha\cos\alpha} + 2r\cos\alpha \\ LL_{S_\varphi} = \|L_{src}, L_{snk}\| \end{cases} \tag{29}$$

3.4.5 User Delay Tolerance Specification

The perimeter of the bounding box can be adjusted based on a user delay tolerance specification. Given that the minimum end-to-end delivery latency T_{min} is dictated by the distance between the source and sink nodes, the user can specify the delay tolerance relative to the latency along the shortest path. This specification method is preferred as the lower bound on the end-to-end latency can vary greatly due to particular proximity of a source node to the corresponding sink. Accordingly, the user may specify the tolerance of end-to-end delivery latency *increase* relative to the shortest absolute end-to-end latency. If we denote $\delta_t \geq 1$ as the relative tolerance specification, the maximum admissible delivery latency acceptable by the user is $T_{max} = \delta_t T_{min}$. Correspondingly, the following relation holds true:

$$\delta_t = \frac{LU_{S_\varphi}}{LL_{S_\varphi}} = \frac{1}{\sin\alpha} + \frac{2r}{\|L_{src}, L_{snk}\|}\left(\frac{1}{\sin\alpha\cos\alpha} + \cos\alpha\right) \tag{30}$$

Relation 30 represents the fundamental relationship between the user delay tolerance specification and the placement of the virtual charges, under the model considered. Figure 27 charts the dependency between the radial r and angular α placement of the virtual charges, and the expected admissible delay increase tolerance, for various placements of the source and sink nodes. According to these charts, the following important observations can be made: (1) the feasible angular placement domain of the virtual charges is $0^\circ << \alpha << 90^\circ$, because, as it can be observed, $\delta_t \to \infty$ for $\alpha \to 0$ or $\alpha \to \pi/2$; (2) α and r represent control parameters for the perimeter of the bounding box to match user delay tolerances.

Given a user tolerance specification and a pair of source-sink charges, Algorithm 6 specifies the recommended strategy for calibrating the sub-field based on the user delay increase tolerance specification δ_t. The strategy is based on the following desideratum: maximize the span-area for the lifetime-critical regions around the source/sink nodes, which are directly controlled by the radial parameter r of the location of the virtual charges, as illustrated in Figure 26. Accordingly, the strategy consist of identifying the angular position of the virtual charges that requires farthest placement along the radial dimension that allows satisfiability of δ_t. To enable this, based on relation 30, the dependency of the radial placement r on the placement of the source and sink nodes, tolerance δ_t and angular placement α can be

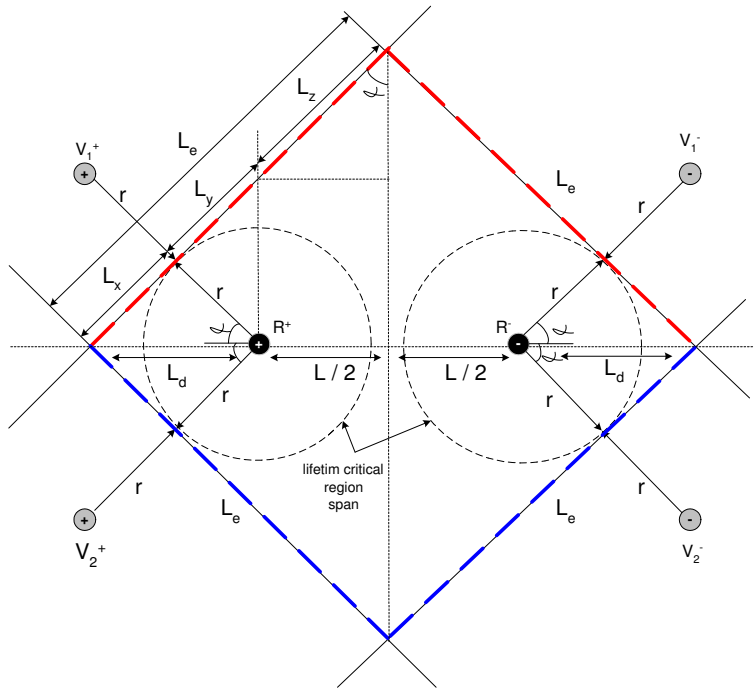

Figure 26: Symmetric bounding sub-field with virtual charges located at (α, r) in the polar coordinate system; parameter r can be used to control the span of the lifetime-critical regions in the vicinity of source/sink nodes

specified through a function $f_r(L_{src}, L_{snk}, \alpha)$ as follows:

$$r = f_r(L_{src}, L_{snk}, \alpha) = \frac{\|L_{src}, L_{snk}\|}{2} \cdot \frac{\delta_t \sin\alpha - 1}{\sin\alpha\cos\alpha + \frac{1}{\cos\alpha}} \tag{31}$$

Algorithm 6 is an instance of a binary search, with an expected logarithmic run-time performance. Placed in the context of the charts in Figure 27, the algorithm effectively searches for the appropriate angular placement of the virtual charges that will allow maximization of the radial parameter r. It is important to note that this algorithm needs to be executed only once for each query submitted, prior to route establishment phase of the MP-FPR protocol, and the results can be locally cached at the source node for subsequent reference. Subsequently, both r and α parameters must be embedded in the body of the RREQ messages in order to enable constructions of QoS enabled routes.

3.5 Experimental Evaluation

In this section we experimentally compare the energy consumption patterns and lifetime performance of MP-FPR protocol with the current state of the art, EFR. The analysis considers the possible impact of various network settings, such as:

- density of sensor nodes
- distribution of sensor nodes in the network
- end-to-end path diversity

under sustained network load, via long-running queries

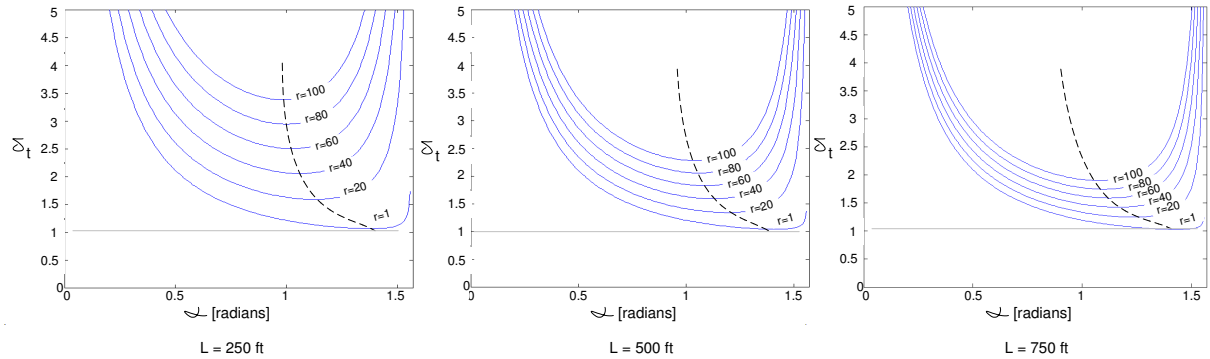

Figure 27: Delay tolerance charts for three different placements of a source and sink node pair: at $250\,ft$, $500\,ft$ and $750\,ft$ apart

Algorithm 6 Bounding Box Calibration; Determining the Coordinates of the Virtual Charges

Input:
$L_{snk}, \{L_{src}\}$: source and sink node location information
δ_t: user latency increase tolerance specification,
ε: calibration accuracy
Output:
α - angular coordinate of the virtual charges
r - radial coordinate of the virtual charges
Algorithm:

```
L ← ||L_src, L_snk||
L_α ← 0        // lower limit
U_α ← π/2      // upper limit
r_prev = 0
α = (U_α + L_α)/2
r ← f_r(L_src, L_snk, α) // cf. relation 31
while |r − r_prev| > ε do
    if r > r_prev then
        L_α ← α
    else
        U_α ← α
    end if
    α = (U_α + L_α)/2
    r ← f_r(L_src, L_snk, α)
end while
```

3.5.1 Simulation Settings

The experiments were performed using the SIDnet-SWANS simulator [22, 1] for WSN. SIDnet-SWANS is an open-source large scale sensor network simulator, which facilitates fast algorithmic implementation on a sensor network comprising a large number of sensor nodes. SIDnet-SWANS is built on the scalable architecture of JiST-SWANS [2], which in turn is based on a high-performance JiST (Java in Simulation Time) engine. When compared to other popular options for sensor network simulation such as ns-2, SIDnet-SWANS enabled us to prepare and perform a large body of experiments in a relatively short amount of time in an environment comprising hundreds of simulated sensor nodes.

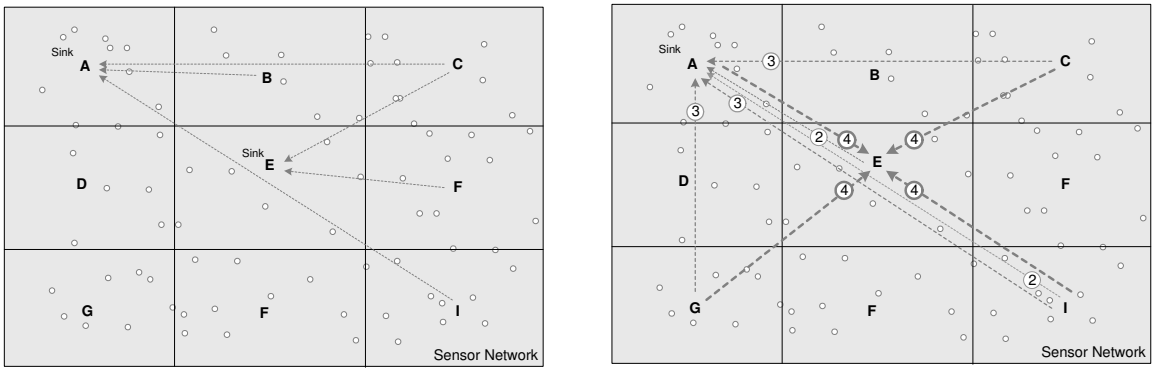

Single-Source Scenarios: C->A, I->A, B->A, C->E, F->E, F->D
(a) using EFR

Multi-Source Scenarios : (2) E, I -> A; (3) C,G,I->A; (4)A,C,G,I->E
(b) using MP-FPR

Figure 28: Deployments utilized for (a) single source and (b) multiple source scenarios. 6 different placements were used for single source. For multi-source, 3 placements –with 2, 3 and 4 sources– were used. Notice that due to symmetry, these placements capture the most representative deployments.

On the other hand, as far as network stack correctness is concerned, it carries adapted version of ns-2's MAC802.15.4 protocol and same signal propagation models.

The simulation consisted of a 750 homogeneous nodes having the following configuration: (i) 20,000 bps transmission/reception rate on the MAC802.15.4 protocol, (ii) 5 seconds idle-to-sleep interval (i.e., nodes not along an active route go to sleep after 5 seconds of idle time, to preserve battery power), and (iii) power consumption characteristics based on the Mica2 Motes specs. To reduce the simulation time, while preserving the validity of the observations, a small fully-charged battery with an initial capacity of 35 mAh powered each node. This battery load projects a lifespan of several tens of hours under moderate load. The evaluations focus on long-term continuous queries (transferring of large amounts of data).

The experimental evaluation concerning the impact of node density variations corroborated with various path diversity instances consists of the following scenarios. We configured 6 single-source and 3 multi-source scenarios, as illustrated in Figure 28. Each scenario was tested for 2 densities (25 and 12 neighbors per node, on average) and for 3 different number of paths between source(s) and sink (15, 30 and 50 paths) as a path diversity property. Each tuple [scenario (9), density (2), number of paths (3)] was tested on 30 different random and uniformly distributed deployments, resulting in a total of 1620 experiments.

It is important to remark that in our simulation setup, we vary the network density by adjusting the length of the sensing area rather than changing the power of the transceiver of individual nodes, in order to maintain consistency across simulations with respect to energy consumption.

3.5.2 Impact of Network Density on Network Lifetime

We reiterate EFR's main weakness: the number of paths is limited by the number of neighbors. This leads to energy-imbalances, and as a consequence, shorter network lifetime.

Figure 29 depicts scenarios where the number of paths is 50 (greater than the average number of neighbors of source/sink nodes). The bars represent the average over all single and multiple source deployments (i.e. over 180 instances for single-source and 90 instances for multi-source).

There are different definitions of the concept of a lifetime [14] in WSN and in our experiments we focused on the following three criteria: – the time until the very first node dies; – the time until 5% of the nodes die; – the time until 10% of the nodes die. Figure 29 gives a break-down on these 3 different network lifetime metrics. Namely, for a lifetime metric of 10% of dead nodes and a density of 12 nodes per neighbor, MP-FPR achieves 6.8 hours (40%) of additional lifetime in single source scenarios, and 3.7 hours (35%) in multiple source scenarios. When the lifetime metric is reduced to 5% of dead nodes or to the first dead node, the improvements are even higher for single source scenarios (60%). This proves the effectiveness of field-persistent forwarding in unmerging paths in spite of the initial

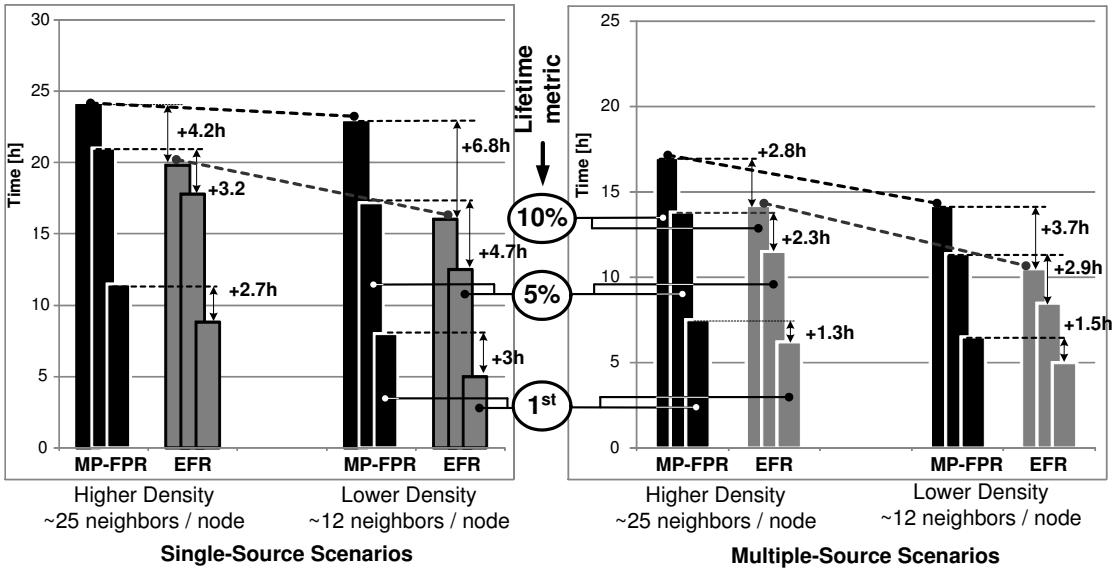

Figure 29: Impact of network density on lifetime. For a density of 12 neighbors per node, MP-FPR performs significantly better than EFR. As the density increases, the difference in performance decreases.

limitation imposed by the number of neighbors.

When the density of the network increases to 25 neighbors per node, the difference between EFR and MP-FPR decreases (between 15% and 30% for single source, and 20% for multiple sources). This occurs due to the fact that path-merging effects decrease as the density increases.

Figure 29 also shows that the lifetime of both routing schemes degrade with reduced network density. This happens because in sparser networks the path-length increases and consequently more energy is consumed on each end-to-end transmission (recall that the density is modified by extending the area instead of decreasing the transmission range).

3.5.3 Impact of Path Diversity on Network Lifetime

We now present the impact of *path diversity* on the lifetime of the network. Figure 30 gives a break-down of network lifetime metrics under 15, 30 and 50 routes in single-source and multi-source settings for a density of 12 neighbors per node.

One of the key motivations of multi-path routing is that a larger number of allowable routing paths should yield better energy load-balancing, and consequently, better lifetimes. However, Figure 30 shows that increasing the number of paths has negligible effects on EFR because in all cases the number of paths is already greater than the number of neighbors of the source nodes, which limits the effective paths used in EFR. On the other hand, MP-FPR shows an improvement when the number of paths is increased from 15 to 30, but not a significant improvement from 30 to 50. This happens because there exists a maximum number of admissible paths, a *saturation point*, beyond which no additional lifetime gain can be obtained, due to finite nodes densities.

The important observation is that the *path saturation point* of path diversity represents an important configuration parameter for field-based routing schemes, and hence should not be considered lightly.The advantage of MP-FPR is that it increases significantly the path-saturation point and hence allows for better load balancing.

3.5.4 Work-load Balancing

We compare load balancing by evaluating the standard deviation of the residual energy of the relay nodes that are involved in routing. Figure 31 shows that for a network density of 12 neighbors per node, on average, MP-FPR achieves significant improvements over EFR in both single-source (68%) and multi-source (56%) scenarios. For a

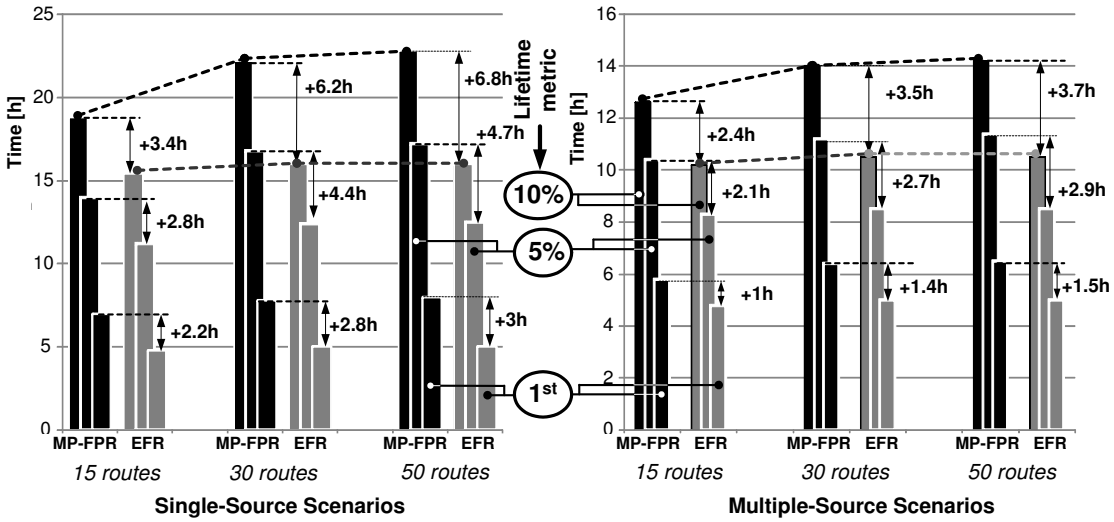

Figure 30: Impact of path diversity on lifetime. For a density of 12 neighbors per node, increasing the number of paths improves the performance of MP-FPR due to its "unmerging" characteristic, while EFR does not benefit from adding more paths.

network density of 25, this difference decreases, confirming the key benefit: due to its "unmerging" characteristic, MP-FPR efficiency increases as the network density decreases. Towards the end of simulation, the overall standard deviation decreases because most nodes' reserves converge towards the residual energy limit (5%).

3.5.5 Impact of Network Discrepancy on Network Lifetime

We continue the experimental evaluation by exploring a different and interesting network dimension: deviation from normal distribution of nodes' placement. Network *discrepancy* is a measure of such deviation, where nodes clustering, i.e. isolated areas of high and low-densities of nodes, may form. We postulate that, in addition to the network density, the discrepancy of nodes distributions represents another measure that can affect the lifetime-performance of the multipath routing. As an illustration, consider Figure 32. It illustrates three different network deployments, all of which having the same density (in terms of the number of nodes in the overall geographic area of interest), but different discrepancy-properties which, in turn, could have a different impact on the routing algorithms performance. This is particularly the case since highly discrepant networks manifest strong local variations in network densities among different regions of the same network, which can accentuate the path merging effects manifested in EFR within sparser regions.

A brief theoretical overview regarding the discrepancy of a point-set is presented next, followed by a reiteration of the node density and path diversity evaluation along the discrepancy dimension.

Discrepancy of a Point Set. Given a d-dimensional unit cube $C^d = [0,1)^d$, the discrepancy of a discrete n-point set $S \subset C^d$ measures how much the distribution of the elements of S deviates from the uniform one [38]. We note that, unlike $d = 1$, in the cases of $d \geq 2$, there may be different criteria of uniformity (e.g., vertices of a square grid vs. equilateral triangles in 2D) and sets that have a good discrepancy for one distribution, may have a bad discrepancy for another. Let $d = 2$ and let *A(R)* denote the area of an axis-parallel rectangle R. The discrepancy of S from the uniform distribution on R, is defined as:

$$D(S,R) = nA(R) - |S \cap R| \tag{32}$$

Letting $\mathcal{R}_2$ denote the collection of all axis-parallel rectangles R, the *discrepancy* of S *over* $\mathcal{R}_2$ is defined as:

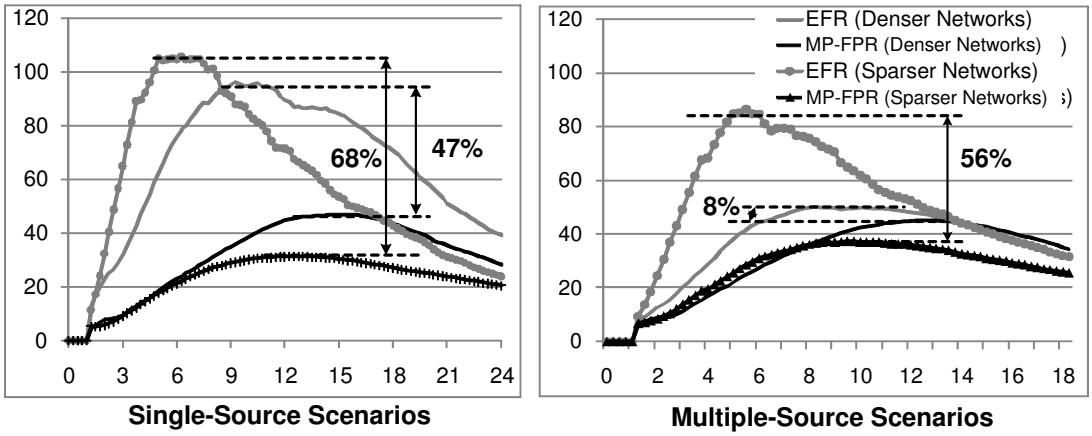

Figure 31: Workload-balancing performance (standard deviation). Given that MP-FPR utilizes a larger fraction of the network to share the communication costs, the energy balance is significantly better in sparser networks.

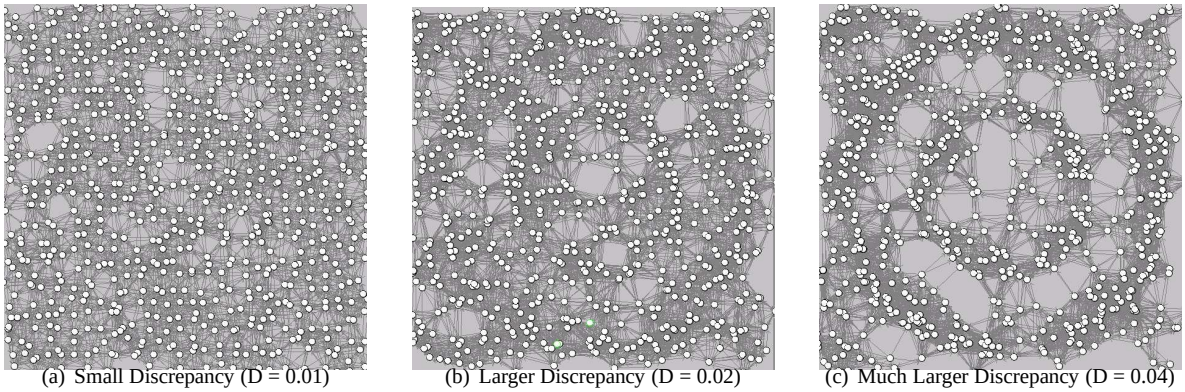

(a) Small Discrepancy (D = 0.01) (b) Larger Discrepancy (D = 0.02) (c) Much Larger Discrepancy (D = 0.04)

Figure 32: Discrepancy of Nodes Distributions

$$D(S,\mathcal{R}_2) = \sup_{R \in \mathcal{R}_2} |D(S,R)| \tag{33}$$

As an illustration, Figure 32 shows three 2D point-sets with different distributions and the corresponding values of the respective discrepancies (cf. [24]), which are actual snapshots of the nodes' locations used for different deployments used during experimental evaluation.

In general, for an n-point set S and another set M, the discrepancy of S with respect to M can be defined as $D(S,M) = |n \cdot A(M \cap [0,1]^2) - |S \cap M||$. Thus, the discrepancy can be also defined as function of n as $D(n,M) = inf(D(S,M))$, where the infimum is taken over all $|S| = n$. We note that, unlike $d = 1$, in the cases of $d \geq 2$, there may be different criteria of uniformity (e.g., vertices of a square grid vs. equilateral triangles in 2D) and sets that have a good discrepancy for one uniform-distribution, may have a bad discrepancy for another.

A plethora of application domains have relied upon results from the discrepancy theory – e.g., numerical integration and complexity theory [11], computer graphics and pattern recognition (super-sampling) [15]. Methodologies have been proposed for computing a discrepancy of a given set, as well as ensuring upper/lower bounds on generated sets [11, 15, 47]. However, this apparatus has not yet been fully utilized in WSN settings and the work comprised in this article only considers it from an experimental evaluation standpoint.

Experimental Setup. Firstly, we considered three different distributions of the nodes' locations (cf. Figure 2), for

which the respective discrepancies' values were 0.01, 0.02, and 0.04, obtained using an implementation of the algorithm in [24]. In addition, the parameter space included: (1) – *density*, in terms of the average number of 1-hop neighbors, with values 8, 12, and 24, obtained by varying the dimensions of the sensing field. The choice of these values was based on approximating the number of neighbors to ensure the connectivity in a random graph (cf. [7, 34]). Although 24 may be too large for practical applications, we wanted to also create settings most favorable for ERF. (2) – *paths diversity*, in terms of maximum allowable alternative source-sink paths: 15, 30 and 50 paths. In the sequel, we present the average of the observation of 50 runs for each parameter-vector (a total of 450 simulations), where we varied the length of the *(sink,source)* distance between 10% and 80% of the diagonal of the rectangle bounding the network, and we used up to 4 sources for a given sink.

		Path Diversity	30								
		Nodes' density	24			12			8		
	Discrepancy	Lifetime Criteria	EFR	MP-FPR	+%	EFR	MP-FPR	+%	EFR	MP-FPR	+%
Single Source	0.01	1st	10.2	11.2	**10%**	8.2	9.8	**20%**	7.5	9.2	**23%**
		5%	16.2	19.8	**22%**	14.5	18.2	**26%**	12	15.2	**27%**
		10%	19.8	22.8	**15%**	16.2	20.8	**28%**	13.8	19.2	**39%**
	0.02	1st	9.5	12.2	**28%**	7.5	9.6	**28%**	4.8	7.2	**50%**
		5%	16.2	19.8	**22%**	12.2	18	**48%**	10	13.2	**32%**
		10%	19.8	22.8	**15%**	15.5	20.2	**30%**	12.2	17.5	**43%**
	0.04	1st	8.8	12.2	**39%**	7	9.2	**31%**	-	-	-
		5%	16.2	19.8	**22%**	10.8	16.8	**56%**	-	-	-
		10%	19.8	22.8	**15%**	14	19	**36%**	-	-	-
Multiple Sources	0.01	1st	7.8	8	**3%**	6	7.2	**20%**	5.5	6.2	**13%**
		5%	11.8	14	**19%**	9.8	11.8	**20%**	8.5	10.2	**20%**
		10%	14	16	**14%**	11.2	13.8	**23%**	10.5	11.8	**12%**
	0.02	1st	7	8.2	**17%**	5	6.2	**24%**	4.5	5.2	**16%**
		5%	12	13.8	**15%**	9.5	11.2	**18%**	7	9	**29%**
		10%	14	16	**14%**	11	13	**18%**	7.8	11	**41%**
	0.04	1st	5.8	6.5	**12%**	5.2	6.2	**19%**	-	-	-
		5%	11	13	**18%**	8.2	9.5	**16%**	-	-	-
		10%	12.8	15.5	**21%**	9.2	11	**20%**	-	-	-

Figure 33: Impact of Density

Load-Balancing. We first present the observations regarding the benefits that MP-FPR yields on the load balancing, in terms of the deviation of the residual energy among the nodes. Figure 34 illustrates the impact of the discrepancy on the load balancing, under medium-density conditions. As it can be seen, consistent benefits of 57% and 50% are recorded in single- and multi-source scenarios under highly discrepant distributions having a discrepancy coefficient of 0.04. Even under very uniform distributions, albeit lower, the benefits of 54% and 36% respectively are still significant. The conclusion is that MP-FPR is significantly less sensitive to deviations of particular nodes distributions than EFR, majorly due to its path-splitting capability.

Network Lifetime. Once again, as a consequence of the better balancing of the residual energy, MP-FPR ultimately yields benefits in terms of prolonging the networks lifetime. Correspondingly, Figure 33 presents a tabular summary of the averaged values of our experimental observations (due to a lack of space, we do not report more detailed results. The columns labelled with "+%" present the benefits of the MP-FPR in terms of percentage increase of the network's lifetime, when compared to the EFR. In all but extremely (unrealistically) dense network scenarios, the single-source settings' benefits of MP-FPR increase with the increase of the discrepancy of the nodes distribution. In multiple sources scenarios, this trend continues to hold in the sparse networks conditions, giving consistently better performances in the other cases. Recall that the reason for considering densities of 24 neighbors per node is to cater the fact that EFR performs best in (theoretically) infinitely dense networks, but degrades significantly in sparser ones. As demonstrated, MP-FPR improves in such trends, which is a key contribution of this work. The scenarios in which the discrepancy is high (0.04) and nodes densities are relatively small (i.e. 8 one-hop neighbors) are extremes, where most of the tested deployments exhibited disconnected topologies, hence we do not report for these settings.

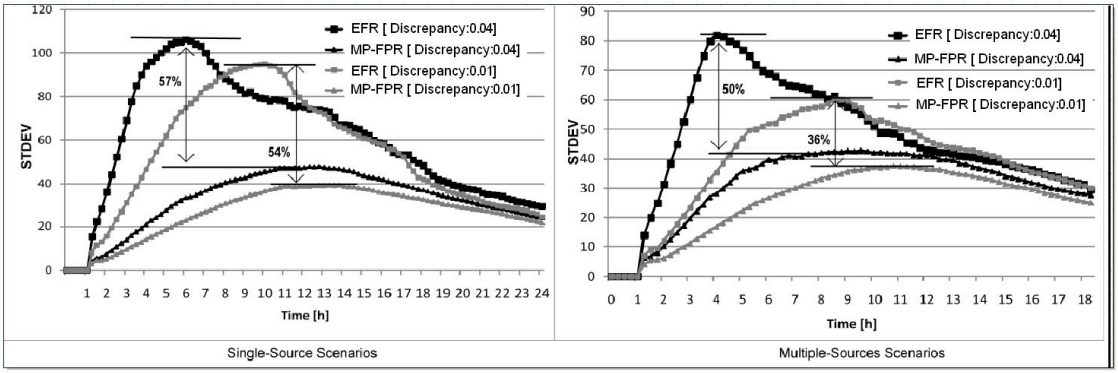

Figure 34: Load-balance vs. Discrepancy

		Nodes' density	12								
		Path Diversity	15			30			50		
	Discrepancy	Lifetime Criteria	EFR	MP-FPR	+%	EFR	MP-FPR	+%	EFR	MP-FPR	+%
Single Source	0.01	1st	7.8	8.8	**13%**	8.2	9.8	**20%**	7.8	10	**28%**
		5%	14	17.2	**23%**	14.5	18.2	**26%**	13.2	18.5	**40%**
		10%	16.2	19.8	**22%**	16.2	20.8	**28%**	16.2	21.2	**31%**
	0.02	1st	7.5	10	**33%**	7.5	10	**33%**	7.5	9.2	**23%**
		5%	13	17.2	**32%**	12.2	18	**48%**	11.8	17.2	**46%**
		10%	15.8	19	**20%**	15.5	20.2	**30%**	15	18.5	**23%**
	0.04	1st	6.8	9.2	**35%**	7	9.2	**31%**	7	9.2	**31%**
		5%	10.8	15.8	**46%**	10.8	16.8	**56%**	11	16.8	**53%**
		10%	14.2	17.5	**23%**	14	19	**36%**	14.2	19.5	**37%**
Multiple Sources	0.01	1st	6.5	7.2	**11%**	6	7.2	**20%**	6.8	7.5	**10%**
		5%	9.8	11.5	**17%**	9.8	11.8	**20%**	9.2	11.8	**28%**
		10%	11.2	13.2	**18%**	11.2	13.8	**23%**	11.2	13.5	**21%**
	0.02	1st	5.8	6.5	**12%**	5	6.2	**24%**	5.8	6.2	**7%**
		5%	10	11.2	**12%**	9.5	11.2	**18%**	9.8	11.2	**14%**
		10%	11.2	13	**16%**	11	13	**18%**	11.2	12.8	**14%**
	0.04	1st	5	6	**20%**	5.2	6.2	**19%**	5	5.5	**10%**
		5%	8.2	11.2	**37%**	8.2	9.5	**16%**	8.2	9.2	**12%**
		10%	9.2	12.8	**39%**	9.2	11	**20%**	9.2	11	**20%**

Figure 35: Impact of Number of Paths

The last set of experiments is summarized in Figure 35, which illustrates the importance of having a broader family of routes used in alternation. As it can be seen, both EFR and MP-FPR benefits from increasing the number of admissible paths, albeit EFR improves marginally beyond the 15 routes mark as the effective number of routes EFR actually uses, due to early path-merging effects, is much lower. However, in both single and multiple source scenarios, MP-FPR reaches a ”plateau” at around 30 admissible paths, beyond which no additional lifetime gains are reported.

3.5.6 Virtual Charges Evaluation

In this Section we experimentally demonstrate the effectiveness of manipulating virtual charges for the purpose of controlling one important QoS metric, namely end-to-end data-packet delivery latency. We specifically study the geographical-proximity impact that virtual charges have over the electrostatic field lines, associated routes and corresponding packet delivery performance. The experimental setup consists of a fixed pair of source and sink nodes and their associated real charges, with a pair of virtual charges positioned around each of them at predefined locations. The experimental investigation has been performed along the two dimensions of a polar coordinate representation of the virtual charges (cf. Figure 23):

- angular coordinate dimension
- radial coordinate dimension

We have performed the evaluation with two sets of source-sink placements, as illustrated in Figure 36. The network consists of 1,250 homogeneous sensor nodes, uniformly distributed in a rectangular area. Experiments have been run under a lower network density setting of 12 neighbors per node conform Section 3.5.3, which achieves an adequate tradeoff between good end-to-end connectivity while preventing high latency variability due to local minima effects found in lesser dense networks. Evaluation along the angular dimension has been performed on an interval between $[15°, 75°]$. The evaluation along the radial dimension has been evaluated over the $[2R_c, 10R_c]$ interval, which covers both proximal as well as distant virtual charges. Each of the placements has been reevaluated 10 times with different node deployment seeds.

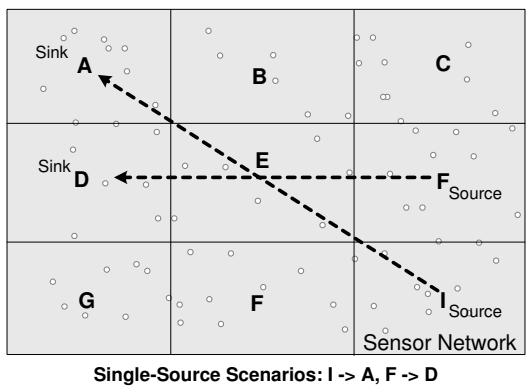

Figure 36: Query setup with two different source-sink queries scenarios for virtual charges evaluation

The experimental evaluation criteria are twofold: (1) we primarily evaluate the impact on the end-to-end packet delivery latency of various virtual charges placement setups, and (2) analyze the energy consumption balancing degradation that the corresponding virtual charges may introduce. For the latter criterion, we have specifically devised three sampling regions within the sensor network to independently assess the impact in the immediate vicinity of source and sink nodes – which represent routing bottlenecks and an energy consumption hot-spots, as well as in mid-network. Figure 37 illustrates these independent assessment regions.

It is important to understand that the amount of control virtual charges provide over the end-to-end packet delivery latencies is not unbounded, and the range of control is given by two factors: (1) network deployment area size, which dictates the upper bound on the end-to-end latencies, and (2) distance between source and sink nodes, which sets the lower bound (i.e. shortest-path routing). Recall that multi-path routing is only possible if a certain latency increase is tolerable as a tradeoff for extended lifetime, and virtual charges are used to provide a mechanism to contain the latency performance within user specified margins. The naive approach to achieve this desideratum is *route suppression*, i.e. route latency probing and subsequent discarding of routes that exceed the performance limits. Such a mechanism can be easily achieved through a TTL-like (Time-To-Live) parameter, which can be used to set the maximum admissible hop-count along a route. Route suppression, however, directly reduces path diversity. As we have demonstrated, poor path diversity is one of the key factors that negatively impact the node utilization around the source and sink nodes, with a direct consequence over the lifetime of the sensor network. Thus, route suppression mechanism is a poor choice for a lifetime-conscious way of controlling QoS metrics such as end-to-end packet delivery latency. As the following experimental results will demonstrate, the containment effect the virtual charges create, in a sense, allows for a more localized path diversity reduction, with a primary impact in mid-network, away from the critical regions surrounding the source and sink/nodes, while maintaining an uniform distribution of routes around the source and sink nodes.

3.5.7 Impact of Virtual Charges' Angular Coordinates

For this test, the radial coordinate has been fixed at an arbitrary point on the assessment interval $[2R_c, 10R_c]$, for example and without loss of generality, at the median point $6R_c$, where R_c represents the communication range. The

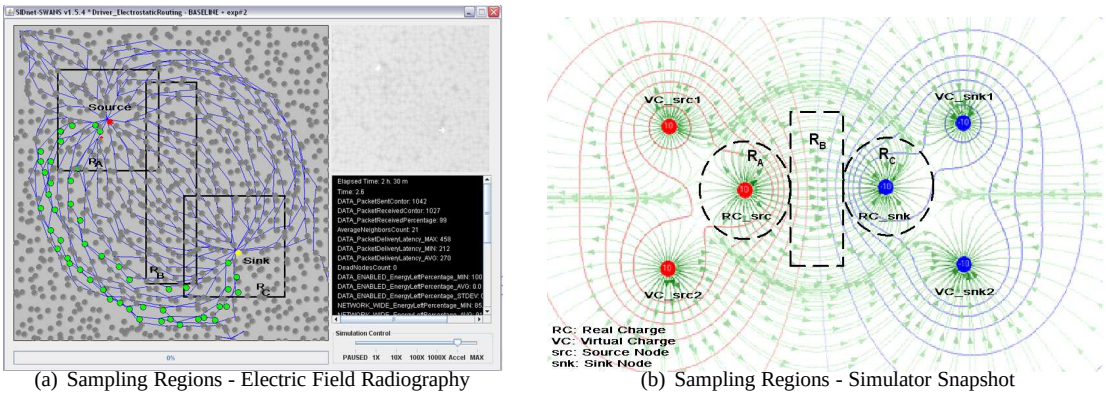

(a) Sampling Regions - Electric Field Radiography (b) Sampling Regions - Simulator Snapshot

Figure 37: Energy Balancing Performance Assessment Regions. Region A - vicinity of the source node; Region B - vicinity of the sink node; Region C - mid-network performance

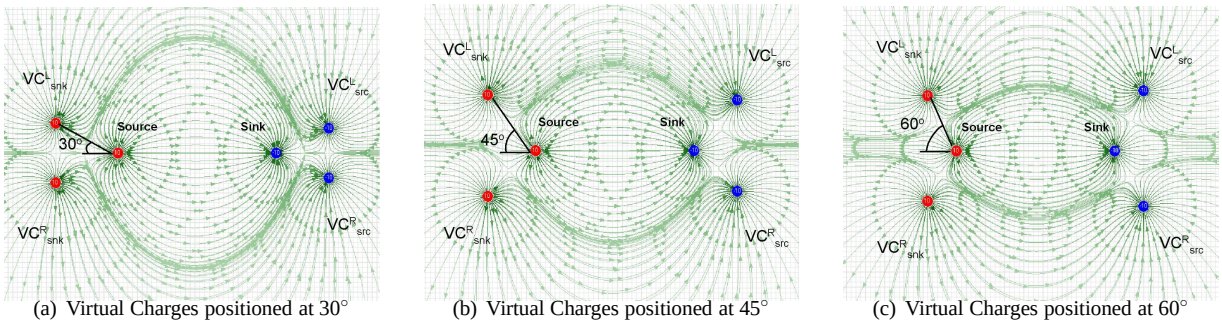

(a) Virtual Charges positioned at 30° (b) Virtual Charges positioned at 45° (c) Virtual Charges positioned at 60°

Figure 38: Field Lines Snapshot Corresponding to Three Angular Assessment Points of Virtual Charges

angular dimension impact has been assessed along the angular interval of $[15°, 75°]$. Figure 38 illustrates the resulting electrostatic field line at three distinct points on the interval, namely 30°, 45° and 60°.

The end-to-end packet delivery latency results are summarized in Figure 39. There are two important aspects of the relationship between the end-to-end packet delivery latency and the angular position of virtual charges to be noted. First, there exists a strong correlation between delivery latencies and the existance/absence of virtual charges altogether in the setup. For example, in the standard MP-FPR setup, i.e. without virtual charges, it can be observed that the latencies are predominantly larger; without virtual charges, these latencies are practically bounded by one factor: network deployment area size, i.e. the longest paths are determined by the boundaries/perimeter of the network. When virtual charges are added, the lengths of the longest paths are reduced due to the containment effect of the virtual charges, thus reducing the length of the corresponding routes. Secondly, there can be seen a quasi-linear relationship between the angular coordinate of the virtual charges and the end-to-end packet delivery latencies. Specifically, delivery latency is inversely proportional to the angular position displacement of the virtual charges. This is a direct consequence of the corresponding reduction of the spread of the contained field lines and associated routes as observed in Figure 38, where shorter field lines are obtained when virtual charges are positioned in the upper range of the assessment interval, i.e. $> 60°$.

Figure 40 captures the energy (im)balance variations as the virtual charges are added, as well as the impact of their specific angular positions. As it can be observed, the impact on the energy consumption patterns is reduced and is, again, dictated by the amount of end-to-end packet delivery latencies reduction one intends to achieve. This trade-off can be observed by correlating the latency improvement benefit, as illustrated in Figure 39, with the corresponding cost in terms of energy consumption imbalance, as illustrated in Figure 40. For example, for a maximum reduction of 60% of the latency metric, the impact on the energy balancing metric, i.e. standard deviation of energy reserves,

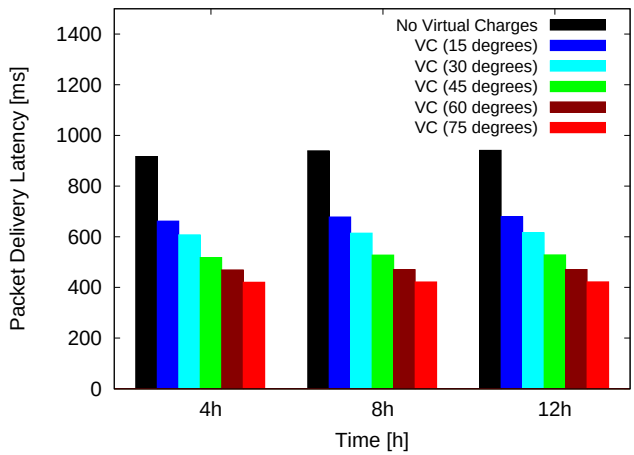

Figure 39: End-to-end packet delivery latency dependency on virtual charges placement along angular dimension

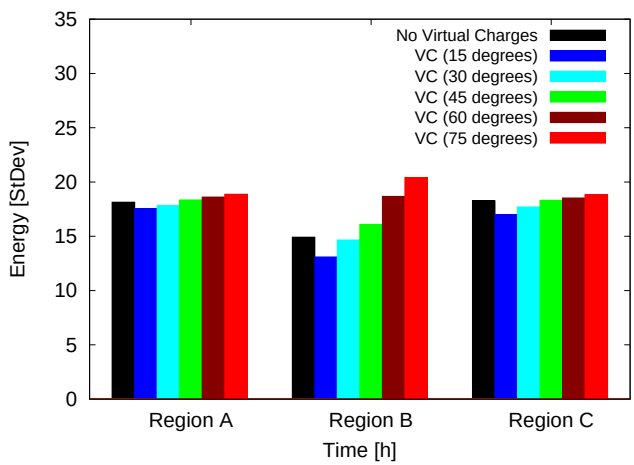

Figure 40: Impact of virtual charges placement along angular dimension over the standard deviation of residual energy levels

is below 5% in the critical regions A and C that surround the source and sink nodes, and below 30% in mid-network. However, for more moderate reduction in packet delivery latencies, which corresponds to virtual charges positioned at 15° and $6R_c$, the delivery latencies are reduced by 30%, while at the same time the energy balancing metric improves by 5% in regions A and C, and by up to 15% in region B. The reason for the improvement is that more field lines are contained within certain lengths limits and thus are usable for routing purposes, increasing path diversity – the main property that promotes energy balancing performance.

3.5.8 Impact of Virtual Charges' Radial Coordinates

For this evaluation, the angular position of virtual charges has been fixed at 45°, and the five experimental assessment points have been defined along the radial coordinate dimension at $2R_c$, $4R_c$, $6R_c$, $8R_c$ and $10R_c$, where R_c represents the communication range. Sample configurations and the corresponding electrostatic field lines are illustrated in Figure 41. As it can be observed, placing virtual charges closer to their corresponding real charges has a containment effect over the field lines and associated routes, leading to shorter end-to-end routes. Clearly, as virtual charges converge towards the location of the source-sink nodes, the maximum packet delivery latencies converge towards the ones given

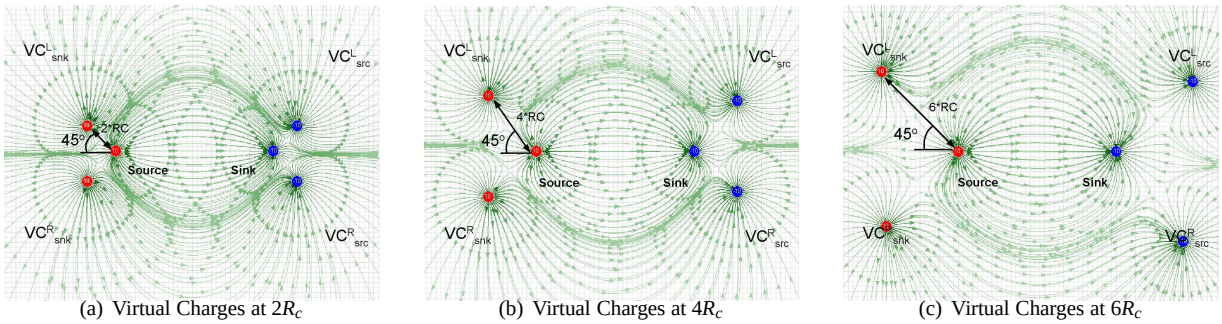

(a) Virtual Charges at $2R_c$ (b) Virtual Charges at $4R_c$ (c) Virtual Charges at $6R_c$

Figure 41: Field Lines Snapshot Corresponding to Three Radial Assessment Points of Virtual Charges

by a shortest path route between the source and sink node. Alternatively, placing the virtual charges farther away relaxes the containment region and increases the path-lengths.

Specifically, Figure 42 confirms the direct dependency of end-to-end packet delivery latencies to variations in placement of virtual charges along the radial dimension. What is interesting to observe, however, is that the level of control achieved not significantly different than along the angular dimension, although the radial dimension does enable control over the entire latency interval, i.e. between lower bound dictated by source and sink locations, and upper latency bound dictated by network bounds, whereas angular dimension is limited by the $[0°, 90°]$ interval of practical applicability.

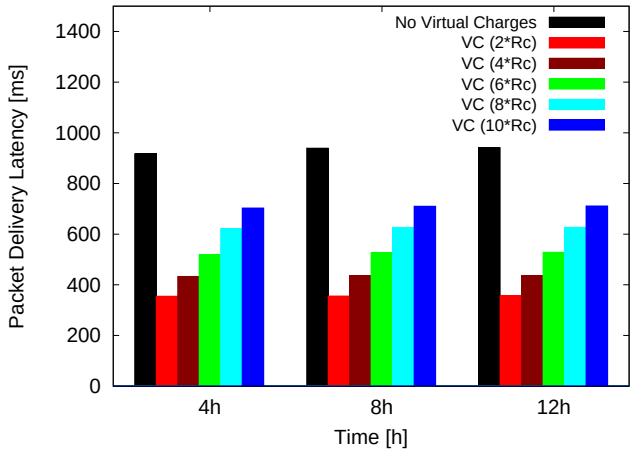

Figure 42: End-to-End packet delivery latency dependency on virtual charges placement along radial dimension

Figure 43 illustrates the impact of virtual charges placement variation along the radial dimension to the energy consumption balancing performance. Although one may observe that the impact is marginally higher under the most latency-restrictive settings, i.e. from an up to 10% in the critical regions A and C surrounding the source and sink nodes, to up to 50% in the mid-network region B, granted that lower delivery latencies are achieved. Disruption of the energy consumption balance in the middle area of the network are expected and are normal, since routes are constrained within a smaller admissible routing region; at an extreme, routes converge towards shortest-path routing type. As opposed to shortest path routing, however, if marginal latency degradation is admissible, significant lifetime extensions can be achieved by placing pairs of virtual charges to: (1) control the latency performance and (2) control the energy consumption balancing primarily in the regions surrounding the source and sink nodes.

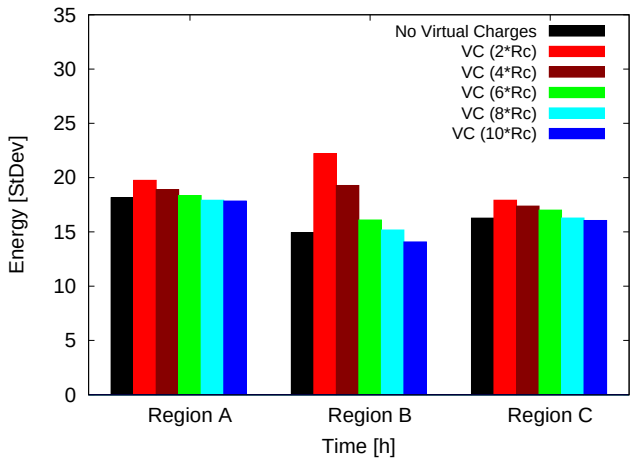

Figure 43: Impact of virtual charges placement along radial dimension over energy consumption balancing performance

4 Related Work

The studies of load balancing in wireless sensor networks (WSN) have had different motivations. One of them is due to the observation that shortest path (and, in general, single-path) routing algorithms unevenly deplete the energy reserves. When source-sink pairs are selected at random, the center of the network handles most of the communication costs, and as a consequence, its energy is consumed at a faster rate [35, 59]. The uneven utilization of energy resources reduces the lifetime of the network and causes holes, however, it has already been demonstrated that achieving a completely balanced energy depletion in WSN settings is, in general, impossible and approaches like q-switch routing were introduced, aiming at sub-balanced energy depletion [58].

Multipath routing has been identified as an option for load balancing, but not just any multipath technique would do. In [21], the authors show that in order to be effective, multipath routing should not select the K-shortest paths but rather select paths that spread the traffic across the network. Based on this insight, several important contributions have been proposed for single-sink single-source scenarios [44, 39, 6, 53, 29]. However, these techniques have a major limitation on single-sink multiple-source scenarios: simultaneous paths between the different sources intersect each other creating severe contention in the wireless medium, imposing overhead on the MAC layer.

In the context described above, the field-based routing has been identified as a paradigm for better load balancing in single-sink multiple-source scenarios. The expanding characteristic of the electric fields allow the spreading of paths across the network, and the attraction-repulsion characteristic of the electric charges determines mutually exclusive routing areas for each source. In [41], Nguyen et al. describe a distributed, stateless, multi-path electrostatic routing scheme (EFR). Their approach demonstrates scalability, robustness, higher delivery ratio and lower overheads when compared to LAR, DREAM, GPSR and AOMDV. However, Nguyen et al. are oblivious to the problem of network boundaries, that is, paths directed towards the borders of the network merge into a single path stressing the use of energy on these nodes.

As for the boundary problem, a centralized solution was proposed by Kalantari *et al.* in [31]. However, the solution requires a-priori information about traffic demands and node positions. By solving a set of partial differential equations, the authors obtain multiple paths without trespassing the boundaries of the network. On a similar line of work, Toumpis and Tassiulas [52] show that the optimal placement of nodes between a set of sources and sinks resembles an electrostatic field. The authors show that their method can also be used to solve boundary problems. Contrary to the centralized solutions of these works, we propose a low-overhead distributed mechanism to cope with boundary effects.

5 Concluding Remarks and Future Work

In this work we addressed the problem of improving network lifetime by balancing the energy-consumption in WSN in the settings. We presented routing methodologies that adapt to the spatial distribution of the neighboring nodes, while taking into account network boundaries effects. We identified techniques for multipath routing in the presence of multiple point-to-point data flows, i.e. multiple sources transmitting towards a given sink. We have introduced a novel mechanism, the method of images, to minimize the path-merging effect at the boundaries of the network. Lastly, we have extended the EFR framework and introduced the concept of virtual charges for the purpose of providing better trade-offs while providing certain QoS guarantees. Our experiments demonstrated that the proposed approaches offer significant benefits when compared to the popular field-based one, such as EFR [41], both in terms of better balancing of the energy reserves, which is the main motivation for multipath routing, as well as increasing the lifetime of a given WSN.

We believe that our current results have barely scratched the surface of exploring the additional benefits that the electrostatic theory can bring to the different research problems of interest in WSNs. Specifically, our algorithms act in a local-best-effort manner to utilize the spatial distribution wherever possible. We have briefly provide insight on how variations of network densities can influence the performance of EFR, while showing the level of resilience to these changes of MP-FPR protocol. Currently, we are envisioning the development of an energy-efficient distributed algorithms that a WSN can use to locally determine such density variations, i.e. local network discrepancy, where the challenging question is how that information can be dynamically maintained (cf. [15]) at different levels of granularity. In this work, we assumed that the initial energy reserves were uniform across the nodes, however, an important problem is how to couple the evolution of the energy reserves with the nodes distribution and how/when to disseminate that information. A potential avenue to explore in this context is to develop abstractions similar to the multidimensional grid files from database research [55].

We also plan to investigate how some of the concepts presented in this work can be cast in other contexts in which field-based routing has been used e.g., optimal attraction regions for networks with multiple sinks [32]; timely and reliable delivery on convergecast applications [25]; routing in networks with mobile sinks [10, 50, 54].

References

[1] http://www.ece.northwestern.edu/ peters/sensors/.

[2] http://jist.ece.cornell.edu/index.html.

[3] Ravindra K. Ahuja, Thomas L. Magnanti, and James B. Orlin. *Network Flows: Theory, Algorithms, and Applications*. Prentice Hall, Englewood Cliffs, NJ, 1993.

[4] K. Akkaya and M. Younis. A survey on routing protocols for wireless sensor networks. *Ad Hoc Networks*, 3(3), 2005.

[5] Junaid Ansari, Dmitry Pankin, and Petri Mähönen. Radio-triggered wake-ups with addressing capabilities for extremely low power sensor network applications. *IJWIN*, 16(3):118–130, 2009.

[6] S.J. Baek and G. de Veciana. Spatial energy balancing through proactive multipath routing in wireless multihop networks. *IEEE/ACM Trans. Netw.*, 15(1):93–104, 2007.

[7] Christian Bettstetter. On the minimum node degree and connectivity of a wireless multihop network. In *MobiHoc*, pages 80–91, 2002.

[8] N. Bulusu, D. Estrin, L. Girod, and J. Heidemann. Scalable coordination for wireless sensor networks: Self-configuring localization systems. In *IN PROCEEDINGS OF THE SIXTH INTERNATIONAL SYMPOSIUM ON COMMUNICATION THEORY AND APPLICATIONS (ISCTA), Ambleside, Lake District, UK, July 2001*, July 2001.

[9] N. Bulusu, J. D. Heidemann, D. Estrin, and T. Tran. Self-configuring localization systems: Design and experimental evaluation. *ACM Transactions on Embedded Computing Systems*, 3(1), 2004.

[10] S.H. Chang, M. Merabti, and HM. Mokhtar. Coordinate Magnetic Routing for Mobile Sinks Wireless Sensor Networks. In *AINAW '07*, volume 1, 2007.

[11] B. Chazelle. *The Discrepancy Method: Randomness and Complexity*. 1998.

[12] Carla-Fabiana Chiasserini and Ramesh R. Rao. Combining paging with dynamic power management. In *INFOCOM, Anchorage, Alaska*, pages 996–1004, 2001.

[13] J. Deogun, S. Das, H. Hamza, and S. Goddard. *An Algorithm for Boundary Discovery in Wireless Sensor Networks*, pages 343–352. 2005.

[14] I. Dietrich and F. Dressler. On the lifetime of wireless sensor networks. *TOSN*, 5(1), 2009.

[15] D.P. Dobkin, D. Eppstein, and D. P. Mitchell. Computing the discrepancy with applications to supersampling patterns. *ACM Trans. Graphics*, 15(4), 1996.

[16] Olivier Dousse, François Baccelli, and Patrick Thiran. Impact of interferences on connectivity in ad hoc networks. *IEEE/ACM Trans. Netw.*, 13(2):425–436, 2005.

[17] L. Fang, W. Du, and P. Ning. A beacon-less location discovery scheme for wireless sensor networks. In *INFOCOM*, pages 161–171, 2005.

[18] Rodrigo Fonseca, Sylvia Ratnasamy, Jerry Zhao, Cheng T. Ee, David Culler, Scott Shenker, and Ion Stoica. Beacon vector routing: Scalable point-to-point routing in wireless sensornets. In *NSDI*, 2005.

[19] Massimo Franceschetti, Olivier Dousse, David N. C. Tse, and Patrick Thiran. Closing the gap in the capacity of wireless networks via percolation theory. *IEEE Transactions on Information Theory*, 53(3):1009–1018, 2007.

[20] Y. Ganjali and A. Keshavarzian. Load balancing in ad hoc networks: Single-path routing vs. multi-path routing. In *INFOCOM*, 2004.

[21] Y. Ganjali and A. Keshavarzian. Load balancing in ad hoc networks: single-path routing vs. multi-path routing. In *INFOCOM 2004*, volume 2, 2004.

[22] O. Ghica, G. Trajcevski, P. Scheuermann, Z. Bischoff, and N. Valtchanov. Sidnet-swans: A simulator and integrated development platform for sensor networks applications. *SenSys*, 2008.

[23] Tian He, Chengdu Huang, Brian M. Blum, John A. Stankovic, and Tarek F. Abdelzaher. Range-free localization schemes for large scale sensor networks. In *MOBICOM*, pages 81–95, 2003.

[24] S. Heinrich. Efficient algorithms for computing l_2 discrepancy. *Mathematics of Computation*, 65(216), 1996.

[25] Hsing-Jung Huang, Ting-Hao Chang, Shu-Yu Hu, and Polly Huang. Magnetic diffusion: disseminating mission-critical data for dynamic sensor networks. In *MSWiM '05*, pages 134–141, New York, NY, USA, 2005. ACM.

[26] Hsing-Jung Huang, Ting-Hao Chang, Shu-Yu Hu, and Polly Huang. Magnetic diffusion: Scalability, reliability, and QoS of data dissemination mechanisms for wireless sensor networks. *Computer Communications*, 29(13-14):2482–2493, August 2006.

[27] Chalermek Intanagonwiwat, Ramesh Govindan, and Deborah Estrin. Directed diffusion: a scalable and robust communication paradigm for sensor networks. In *MOBICOM*, pages 56–67, 2000.

[28] Rajagopal Iyengar, Koushik Kar, and Suman Banerjee. Low-coordination wake-up algorithms for multiple connected-covered topologies in sensor nets. *IJSNET*, 5(1):33–47, 2009.

[29] N. Jain, D.K. Madathil, and D.P. Agrawal. Energy Aware Multi-path Routing for Uniform Resource Utilization in Sensor Networks. *LNCS*, pages 473–487, 2003.

[30] O.D. Jefimenko. *Electricity and Magnetism: An Introduction to the Theory of Electric and Magnetic Fields*. Electret Scientifice, 1989.

[31] M. Kalantari and M. Shayman. Routing in wireless ad hoc networks by analogy to electrostatic theory. In *Communications, 2004 IEEE International Conference on*, volume 7, pages 4028–4033 Vol.7, 2004.

[32] M. Kalantari and M. Shayman. Design optimization of multi-sink sensor networks by analogy to electrostatic theory. In *WCNC 2006. IEEE*, volume 1, pages 431–438, 2006.

[33] L. Kirkup. Computer simulation of electric field lines. *Physics Education, Northern Ireland*, 20, 1985.

[34] B. Krishnamachari, S. B. Wicker, and R. Bejar. Phase transition phenomena in wireless ad-hoc networks. In *In GLOBECOM*, 2001.

[35] S. Kwon and NB. Shroff. Paradox of Shortest Path Routing for Large Multi-Hop Wireless Networks. In *INFOCOM 2007*, pages 1001–1009, 2007.

[36] W. Luo, W. Liu, and Y. Zhang. Performance optimizatin using multipath routing in mobile ad hoc and wireless sensor networks. *Combinatorial Optimization in Communication Networks*, 2, 2005.

[37] A. Manjhi, S. Nath, and P.B. Gibbons. Tributaries and deltas: Efficient and robust aggregation in sensor networks. In *ACM International Conference on Management of Data (ACM SIGMOD)*, 2005.

[38] J. Matousek. *Geometric Discrepancy: an Illustrated Guide*. 1999.

[39] A. Mei and J. Stefa. Routing in outer space: fair traffic load in multi-hop wireless networks. In *MobiHoc '08*, pages 23–32, New York, NY, USA, 2008. ACM.

[40] R. Nagpal, H.E. Shrobe, and J. Bachrach. Organizing a global coordinate system from local information on an ad hoc sensor network. In *IPSN*, pages 333–348, 2003.

[41] N. T. Nguyen, A. Wang, P. Reiher, and G. Kuenning. Electric-field-based routing: a reliable framework for routing in MANETs. *SIGMOBILE Mob. Comput. Commun. Rev.*, 8(2):35–49, 2004.

[42] D. Niculesu and B. Nath. Trajectory based forwarding and its applications. In *MOBICOM*, 2003.

[43] G. Parissidis, V. Lenders, M. May, and B. Plattner. Multi-path routing protocols in wireless mobile and ad hoc networks: A quantitative comparison. In *NEW2AN*, 2006.

[44] L. Popa, A. Rostamizadeh, R. Karp, C. Papadimitriou, and I. Stoica. Balancing traffic load in wireless networks with curveball routing. In *MobiHoc '07*, pages 170–179, New York, NY, USA, 2007. ACM.

[45] Merrill J. R. Using computers in physics. In *Boston: Houghton Mifflin*.

[46] F. Reichenbach, A. Born, D. Timmermann, and R. Bill. A distributed linear least squares method for precise localization with low complexity in wireless sensor networks. In *in Wireless Sensor Networks, IEEE International Conference on Distributed Computing in Sensor Systems (DCOSS06*, 2006.

[47] P. Shirley. Discrepancy as a quality measure for sample distributions. In *Eurographics*, 1991.

[48] V. Srinivasan, P. Nuggehalli, C.-F. Chiasserini, and R. R. Rao. Cooperation in wireless ad hoc networks. In *INFOCOM*, 2003.

[49] Bharath Sundararaman, Ugo Buy, and Ajay D. Kshemkalyani. Clock synchronization for wireless sensor networks: a survey. *Ad Hoc Networks*, 3(3):281–323, 2005.

[50] J. Tateson and I.W. Marshall. A Novel Mechanism for Routing in Highly Mobile Ad Hoc Sensor Networks. *LNCS*, pages 204–217, 2004.

[51] S. Toumpis. Mother nature knows best: A survey of recent results on wireless networks based on analogies with physics. *Computer Networks*, 52(2):360–383, February 2008.

[52] Stavros Toumpis and Leandros Tassiulas. Packetostatics: deployment of massively dense sensor networks as an electrostatics problem. In *INFOCOM*, pages 2290–2301, 2005.

[53] G. Trajcevski, O. Ghica, and P. Scheuermann. CAR: controlled adjustment of routes and sensor networks lifetime. In *MDM 2006*, page 23, 2006.

[54] Z. Vincze, K. Fodor, R. Vida, and A. Vidacs. Electrostatic Modelling of Multiple Mobile Sinks in Wireless Sensor Networks. In *PWSN '06*, 2006.

[55] K.-Y. Whang, S.W. Kim, and G. Wietherhold. Dynamic maintenance of data distribution for selectivity estimation. *VLDB*, 3(1), 1994.

[56] Technische Universitt Wien, Thomas Eiter, Thomas Eiter, Heikki Mannila, and Heikki Mannila. Computing discrete frchet distance. Technical report, 1994.

[57] S. Wu and K. Selçuk Candan. Power-aware single- and multipath geographic routing in sensor networks. *Ad Hoc Networks*, 5(7):974–997, 2007.

[58] X. Wu, G. Chen, and S.K. Das. Avoiding energy holes in wireless sensor networks with nonuniform node distribution. *IEEE Trans. Parallel and Distributed Computing*, 19(5), 2008.

[59] J. Yang and D. Zhang. An energy balancing unequal clustering protocol for wireless sensor networks. *Information Techology*, 8(1), 2009.